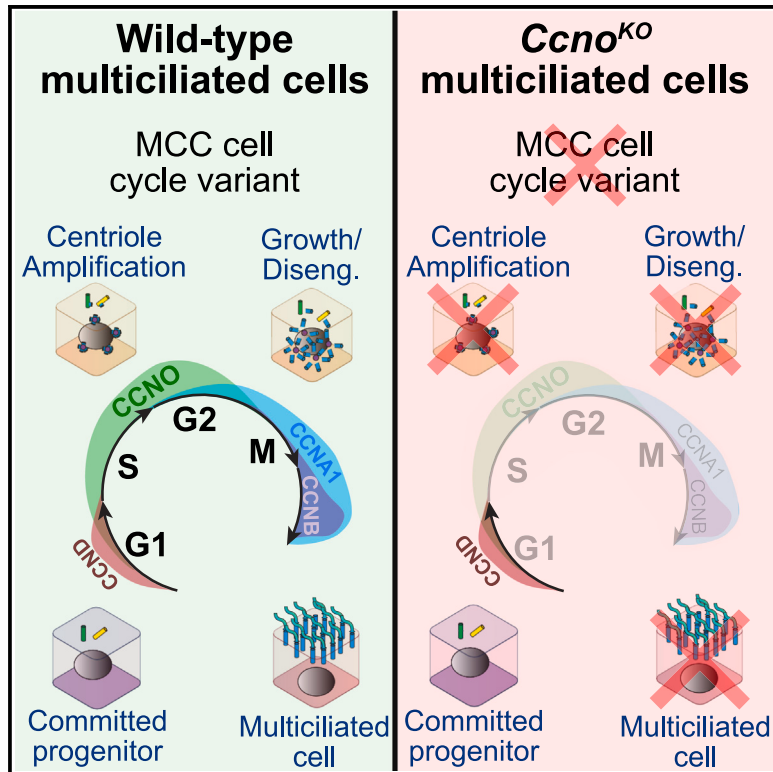


Cyclin O controls entry into the cell-cycle variant required for multiciliated cell differentiation

Graphical abstract



Authors

Michella Khoury Damaa, Jacques Serizay, Rémi Balagué, ..., Sudipto Roy, Nathalie Spassky, Alice Meunier

Correspondence

alice.meunier@bio.ens.psl.eu

In brief

Khoury Damaa et al. show that Cyclin O (CCNO) is required for G₁/S transition of the multiciliated cell-cycle variant and for the consecutive progression of centriole amplification. Human patients suffering from CCNO mutations and mutant mouse brains show a complete lack of centrioles and cilia in multiciliated cells.

Highlights

- CCNO absence blocks the G₁/S transition of the cell-cycle variant of multiciliated cells
- CCNO controls the early onset of centriole amplification, leading to cilia formation
- Human respiratory cells lacking CCNO show a complete lack of centrioles and cilia
- Respiratory cells in mice can partly compensate CCNO absence



Article

Cyclin O controls entry into the cell-cycle variant required for multiciliated cell differentiation

Michella Khouri Damaa,¹ Jacques Serizay,^{1,2} Rémi Balagué,¹ Amélie-Rose Boudjema,¹ Marion Faucourt,¹ Nathalie Delgehyr,¹ Kim Jee Goh,^{3,18} Hao Lu,⁴ Ee Kim Tan,³ Cameron T. James,^{4,5,6} Catherine Faucon,⁷ Rana Mitri,⁷ Diana Carolin Bracht,⁸ Colin D. Bingle,⁵ Norris Ray Dunn,^{3,9} Sebastian J. Arnold,^{10,11} Laure-Emmanuelle Zaragosi,¹² Pascal Barbry,^{12,13} Romain Koszul,² Heymut Omran,⁸ Gabriel Gil-Gómez,¹⁴ Estelle Escudier,^{15,16} Marie Legendre,^{15,16} Sudipto Roy,^{4,17} Nathalie Spassky,¹ and Alice Meunier^{1,19,*}

¹Institut de Biologie de l'ENS (IBENS), CNRS, INSERM, Ecole Normale Supérieure, PSL Research University, Paris, France

²Institut Pasteur, CNRS UMR3525, Université Paris Cité, Unité Régulation Spatiale des Génomes, Paris, France

³Lee Kong Chian School of Medicine, Nanyang Technological University, Clinical Sciences Building, 11 Mandalay Road, Singapore 308232, Singapore

⁴Institute of Molecular and Cell Biology, Agency for Science, Technology and Research, Proteos, 61 Biopolis Drive, Singapore 138673, Singapore

⁵Division of Clinical Medicine, School of Medicine and Population Health, University of Sheffield, Sheffield S10 2RX, UK

⁶Singapore-MIT Association for Research and Technology, Critical Analytics for Manufacturing Personalised-Medicine (SMART CAMP), 1 CREATE Way, Singapore 138602, Singapore

⁷Centre Hospitalier Intercommunal de Crétteil, Laboratoire de Microscopie Électronique, Service d'Anatomopathologie, 94010 Crétteil, France

⁸Department of General Pediatrics, University Hospital Muenster, 48149 Muenster, Germany

⁹Skin Research Institute of Singapore, 11 Mandalay Road #17-01 Clinical Sciences Building, Singapore 308232, Singapore

¹⁰Institute of Experimental and Clinical Pharmacology and Toxicology, Faculty of Medicine, University of Freiburg, Albertstrasse 25, 79104 Freiburg, Germany

¹¹Signaling Research Centers BIOSS and CIBSS, University of Freiburg, Schänzlestrasse 18, 79104 Freiburg, Germany

¹²Université Côte d'Azur, CNRS, Institut de Pharmacologie Moléculaire et Cellulaire, 06560 Sophia Antipolis, France

¹³IIA Côte d'Azur, 06560 Sophia Antipolis, France

¹⁴Hospital del Mar Research Institute, Doctor Aiguader 88, 08003 Barcelona, Spain

¹⁵Sorbonne Université, Inserm, Childhood genetic diseases UMR_S933, Hôpital Armand-Trousseau, 75012 Paris, France

¹⁶AP-HP, Sorbonne Université, Hôpital Armand-Trousseau, 75012 Paris, France

¹⁷Department of Pediatrics, Yong Loo Lin School of Medicine, National University of Singapore, 1E Kent Ridge Road, Singapore 119288, Singapore

¹⁸Present address: Hoxton Farms, HYLO Building, 105 Bunhill Row, London EC1Y 8LZ, UK

¹⁹Lead contact

*Correspondence: alice.meunier@bio.ens.psl.eu

<https://doi.org/10.1016/j.celrep.2024.115117>

SUMMARY

Multiciliated cells (MCCs) ensure fluid circulation in various organs. Their differentiation is marked by the amplification of cilia-nucleating centrioles, driven by a genuine cell-cycle variant, which is characterized by wave-like expression of canonical and non-canonical cyclins such as Cyclin O (CCNO). Patients with CCNO mutations exhibit a subtype of primary ciliary dyskinesia called reduced generation of motile cilia (RGMC). Here, we show that *Ccno* is activated at the crossroads of the onset of MCC differentiation, the entry into the MCC cell-cycle variant, and the activation of the centriole biogenesis program. Its absence blocks the G₁/S-like transition of the cell-cycle variant, interrupts the centrilogenesis transcription program, and compromises the production of centrioles and cilia in mouse brain and human respiratory MCCs. Altogether, our study identifies CCNO as a core regulator of entry into the MCC cell-cycle variant and the interruption of this variant as one etiology of RGMC.

INTRODUCTION

Multiciliated cells (MCCs) propel physiological fluids within the lumen of several fluid-producing organs. In the brain ventricles, they contribute to the flow of cerebrospinal fluid; in the respiratory tract, they are necessary for mucociliary clearance; and in

the female and male reproductive tracts, they contribute to the movement of eggs and sperm, respectively.^{1–4} A key event during MCC differentiation is the massive amplification of centrioles, which then mature as basal bodies for nucleating tufts of motile cilia. Although MCCs from different tissues do not share the same cell lineage, the molecular cascade that regulates centriole



amplification seems well conserved and shares similarities with the centriole duplication program during the cell cycle. This process requires critical centriolar assembly proteins such as PLK4 and SAS6^{5–7} and master cell-cycle regulators such as cyclin-dependent kinase 1 (CDK1), CDK2, PLK1, and APC/C that control centriole number and maturation.^{8–10} In a companion study on mouse brain MCCs,¹¹ we further show that besides these regulators, the majority of cell-cycle players are re-expressed and orchestrate a cell-cycle variant progressing through S-, G₂-, and M-like phases and tailored with wave-like expression of canonical and non-canonical cyclins during MCC differentiation. This cell-cycle variant is also conserved in various mouse tissues^{11,12} and seems conserved in human airways.¹¹

The contribution of Cyclin O (CCNO)—the first non-canonical cyclin expressed during this cell-cycle variant—to MCC differentiation was first discovered in human patients with mutations in the CCNO gene. These patients suffer from a distinctive form of primary ciliary dyskinesia (PCD) referred to as reduced generation of multiple motile cilia (RGMC) because of cilia rarity in the airway epithelium.^{13–18} In parallel, an in-depth study of airway MCCs from *Ccno* mutant mice showed a disorganized amplification of centrioles, ultimately resulting in incomplete multiciliation (Funk et al.,¹⁹ *Ccno*^{RA}). Similarly, in the multiciliated epidermis of *Xenopus* larvae, a surrogate model of mammalian MCC-bearing epithelia, morpholino-mediated inhibition of CCNO function results in a reduced number of centrioles and cilia.^{13,18} Although not comprehensively studied at the cellular level, the phenotype appears similar in the oviducts of full *Ccno* knockout mice, with a decrease in the number of cilia per cell,²⁰ and in the efferent ducts of the testes, where a loss of multiciliation is observed.³ In mouse brain, the cellular phenotype appears more severe but is not quantified.²⁰

The clinical phenotype of patients suffering from RGMC with CCNO mutations unequivocally defines CCNO as a determinant for MCC function. However, the cellular phenotype of CCNO depletion varies from a delayed and defective centriole amplification leading to partial multiciliation to a total absence of cilia, depending on how CCNO is depleted, the cellular model, and the species examined.^{3,18–20} Moreover, the mechanism of action of CCNO in the MCC differentiation program remains unknown. Here, using two mouse models for *Ccno* loss of function, as well as airway MCCs derived from human embryonic stem cells (hESCs) and nasal biopsies from patients suffering from PCD with CCNO mutations, we show that: (1) a subpopulation of airway MCCs from *Ccno* mutant mice can amplify centrioles, albeit abnormally, while human airway MCCs cannot; (2) mouse brain MCCs display a phenotype comparable to that of human airway MCCs, where centrioles are not produced in the absence of CCNO; and (3) CCNO controls centriole amplification by regulating entry into the MCC differentiation cell-cycle variant.

RESULTS

Mutated *Ccno* progenitors fail to develop into MCCs in the mouse brain compared to the mouse trachea

Discrepancies between cellular models in the literature prompted us to test whether a differential phenotype could exist between brain and airway MCCs from mice without CCNO. Human

and mouse CCNO proteins share similarities with other canonical cyclins such as CCNA, CCNB, and CCNE (Figure S1A). The *Ccno* locus is overall well conserved across vertebrates, exhibiting collinearity with *Mcidas* immediately downstream of *Ccno*, although we note that *Ccno* and *Mcidas* collinearity is absent in zebrafish (Defosset et al.²¹; Figure S1A). We first leveraged the *Ccno*^{RA} mouse model, where 2 out of 3 exons of *Ccno* are lacking (Figure S1B, Funk et al.¹⁹), and performed whole-tissue immunostaining of glutamylated tubulin (GT335) to detect multiple cilia of MCCs and the primary cilium of other cell types including MCC progenitors from samples of both lateral ventricular walls of the brain and trachea. To circumvent individual variability, we compared brain and airway epithelia dissected from the same individuals at postnatal day 35 (P35), when MCC differentiation is complete in both tissues. As previously published,¹⁹ we observed MCCs in *Ccno*^{RA} tracheal tissues, albeit more scarcely distributed than in the controls. However, in the same individuals, MCCs are very rarely observed in brain lateral ventricular walls (LVW), while they cover the whole LVW in the brains of control animals (Figure S1C).

To test whether the truncated CCNO protein that could potentially be translated in the *Ccno*^{RA} model could be responsible for the partial multiciliation observed in tracheal tissues, we then leveraged mutants with a complete deletion of the *Ccno* gene locus (*Ccno*^{KO}, Figure S1B; Núñez-Ollé et al.²⁰). Here again, almost no MCCs were observed in the brain, while in the trachea of the same individuals MCCs can still be formed, albeit with approximately 70% reduction compared to controls (Figures 1A and 1B). In the mutants' brain, the few MCCs produced have an abnormal morphology, with very few cilia. In the trachea, however, half of MCCs present a seemingly normal morphology while the other half present more scarcely distributed multiple cilia, as previously described in mouse *Ccno*^{RA} respiratory cells (Figures 1C and 1D; Funk et al.¹⁹).

Altogether, this shows that in both *Ccno* mutants, a differential phenotype exists between brain and tracheal MCCs, which suggests that in mouse, CCNO is essential for MCC formation in the brain, while its absence can be partially compensated for in the tracheal tissues. Due to the wide range of severe clinical manifestations of patients with CCNO mutations,¹³ we decided to further assess the function of CCNO in MCC differentiation using mouse brain MCCs as a model system.

CCNO stands at the crossroads between MCC differentiation, MCC cell-cycle variant, and centriole amplification pathways

We sought to identify the molecular and cellular processes of MCC differentiation that are controlled by CCNO. We first performed immunostaining for CCNO protein during *in vitro* differentiation of MCC brain progenitors. We found that CCNO protein is absent before the onset of centriole amplification, when progenitors display a single centrosome (labeled by FOP). CCNO is then detected as cells enter the amplification "A" phase, when procentrioles amplify, and during the growth "G" phase, when procentrioles mature, with enrichment in the nuclear compartment. Eventually, CCNO is sharply reduced in both cell compartments during the disengagement "D" phase, when centrioles begin to disengage from their growing platforms, the deuterosomes,

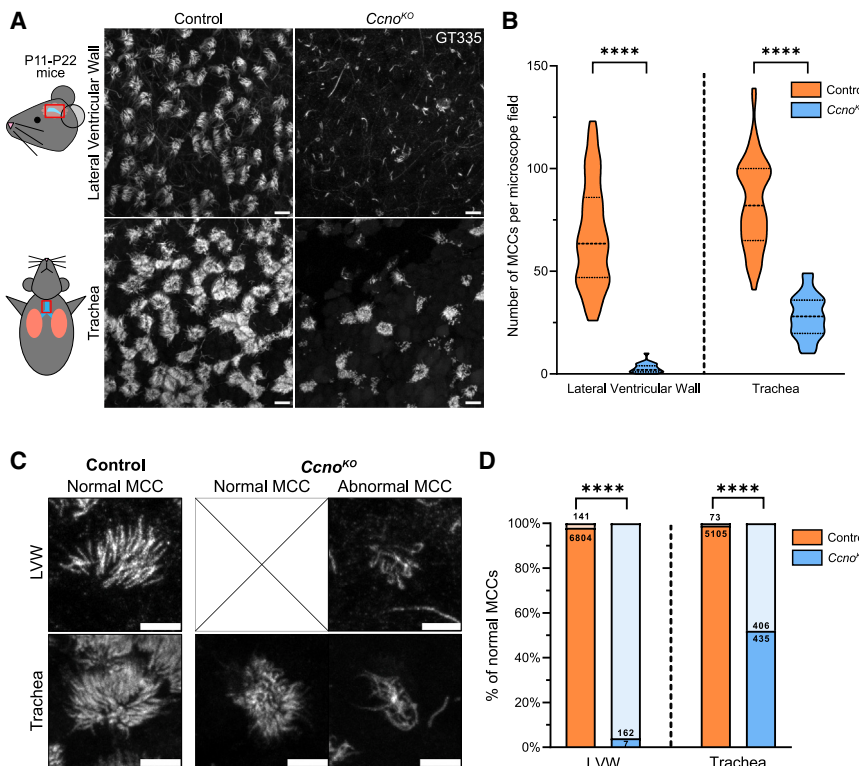


Figure 1. Mutated *Ccno* progenitors fail to develop into MCCs in the mouse brain compared to the mouse trachea

(A) Immunostaining of control and *Ccno*^{KO} mice lateral ventricular wall (LVW) of the brain and trachea dissected from the same animal at P22, with polyglutamylated marker GT335 for cilia. Scale bars, 10 μ m.

(B) Quantification of MCCs per microscope field in both LVW and trachea of P11 to P22 mice. Images from 12 control mice and 6 *Ccno*^{KO} mice were quantified, with 3–6 images per immunostained tissue. Control LVW, 100 values; *Ccno*^{KO} LVW, 60 values; control trachea, 59 values; *Ccno*^{KO} trachea, 30 values. p values are derived from two-tailed Mann-Whitney U test, *** p < 0.0001. The violin plots represent the distribution of values; the dashed horizontal line shows the median value, and the dotted horizontal lines show the interquartile range.

(C) The few MCCs found in the brain are almost all abnormal in the *Ccno*^{KO}, with very few and disorganized cilia per cell, as shown by upper panels. In the *Ccno*^{KO} trachea, half of the formed MCCs have a normal morphology; the rest is abnormal, as indicated by the bottom panels. Scale bars, 5 μ m.

(D) Quantification of normal MCCs in both LVW and trachea of P11–P22 mice in the same images quantified for (B). p values are derived from two-sided chi-squared test (two-proportion Z test), *** p < 0.0001.

See also Figure S1.

and until multiciliation (Figures 2A, 2B, and S2A; Al Jord et al.⁸). CCNO seems to be mostly nuclear located as shown by the intensity ratio of nuclear/cytoplasmic signal in A and G phases (Figure 2B).

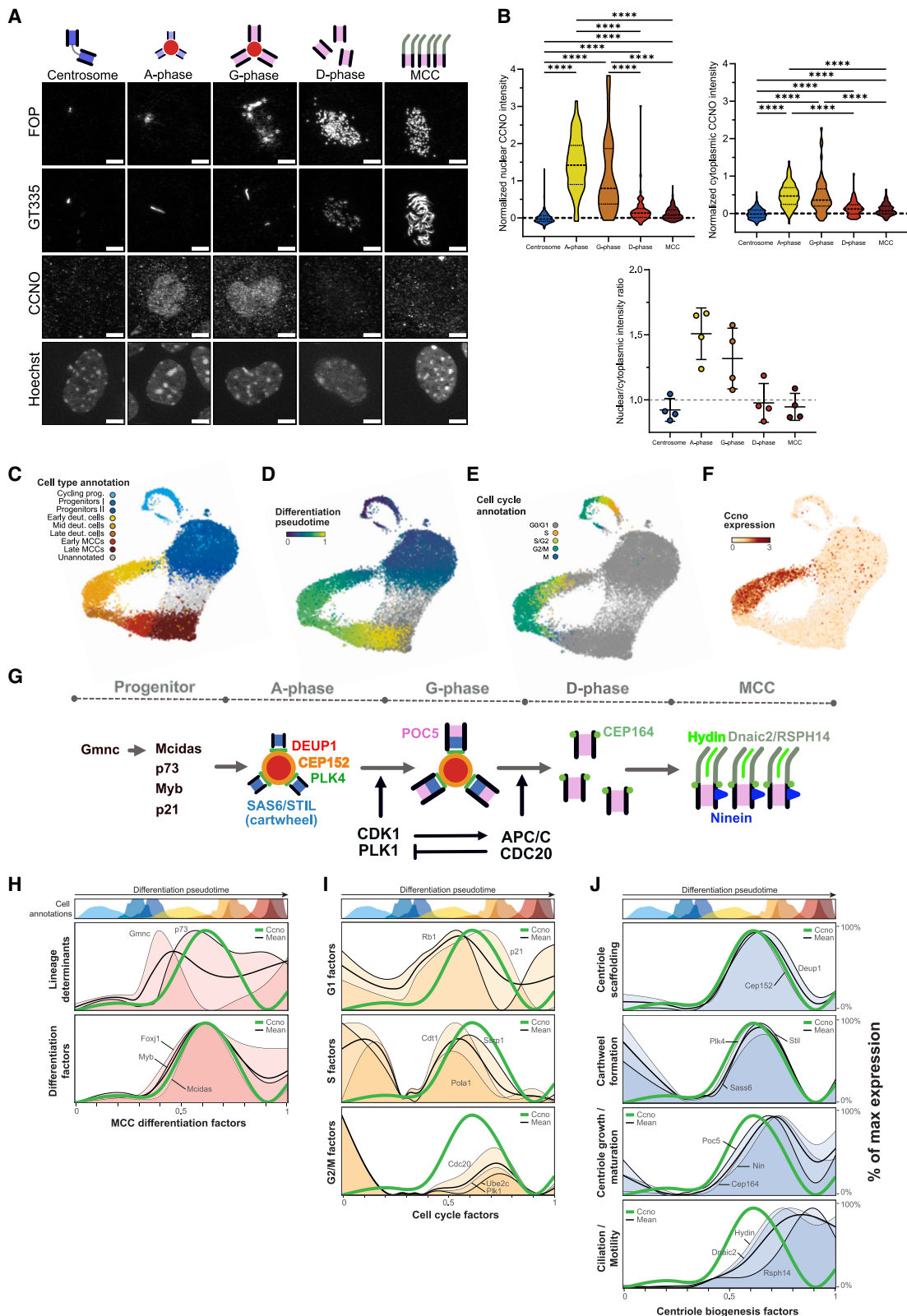
To further refine the context in which *Ccno* is expressed, we leveraged the MCC differentiation lineage pseudotime inferred from the single-cell transcriptomics dataset described in Serizay et al.,¹¹ comprising (1) cycling and quiescent brain MCC progenitors, (2) differentiating MCC progenitors (identified as early, mid, and late deuterosomal cells), and (3) terminally differentiated MCCs (Figures 2C–2E). In this continuous transcriptional landscape and consistent with immunostaining data, *Ccno* is not expressed in MCC progenitors, is activated in the early and mid-deuterosomal cell clusters, and is then silenced along the rest of the differentiation process (Figures 2C–2F). Cell-cycle phase annotations from neural stem cell single-cell RNA sequencing (scRNA-seq)²² detects *Ccno*-expressing cells as progressing from G₀/G₁- to S/G₂- and G₂/M-like phases of the cell cycle (Figure 2E). Finally, we show in our associated study¹¹ that *Ccno* expression is temporally correlated with the expression of centriole biogenesis core components.

We further analyzed the temporality of *Ccno* expression compared to core regulators of (1) MCC fate determination, (2) MCC cell-cycle variant, and (3) centriole biogenesis. First, the temporality of expression of MCC fate determinants is consistent with functional studies^{23,24} where the lineage determinant *Gmnc* is expressed first, specifically in the progenitor and early deuterosomal clusters, followed by *Myb*, involved in multilineage airway epithelial cell differentiation²⁵ expressed from late-pro-

genitor to mid-deuterosomal clusters. *Foxj1* is also upregulated in the progenitor clusters but remains expressed during the whole differentiation process, consistent with its role in late events during MCC differentiation. Finally, transcription factor p73 expression occurs early on in the early deuterosomal cluster, whereas *Mcidas* is expressed slightly later, in early- and mid-deuterosomal clusters (Figures 2G, 2H, and S2B). In this transcriptional landscape and consistent with identifying *Ccno* as a Myb-regulated gene,²⁵ *Ccno* activation and duration of expression is comparable to that of *Myb* from late-progenitor to mid-deuterosomal clusters. Unexpectedly, however, *Ccno* activation seems to occur slightly before *Mcidas* (Figures 2G, 2H, and S2D).

Within the MCC cell-cycle variant, and consistent with cell-cycle phase annotations, the onset of *Ccno* expression is consecutive to the activation of typical G₁ factors (*Cdkn1A* [p21] and *Rb1*), is concomitant with S factors (*Cdt1*, FACT complex subunit *Ssrp1*, and the catalytic subunit of DNA polymerase alpha [*Pola1*]), and precedes and overlaps the activation of factors involved in mitotic progression (*Plk1*, *Ube2c* subunit of APC/C, APC/C cofactor *Cdc20*). These cell-cycle core regulators are silenced before or, eventually, concomitantly with *Ccno* (Figure 2I).

Finally, concerning the centriole biogenesis molecular subprocesses, *Ccno* activation is concomitant with the centriole scaffolding genes *Deup1* and *Cep152* and slightly precedes the expression of cartwheel components *Plk4*, *Stil*, and *Sass6*. The duration of expression of all these early genes is comparable with that of *Ccno*. The onset of expression of genes involved in centriole growth and maturation (*Poc5*, *Cep164*, and *Ninein*) occurs later and continues after *Ccno* silencing. Finally, the motile



(legend on next page)

cilia genes *Dnaic2*, *Hydin*, and *Rspn14* are expressed later, only partially overlapping with decreasing expression of *Ccno* (Figures 2J and S2C).

Together, these observations highlight the strategic temporal window during which *Ccno* is activated, at the crossroads between the onset of MCC differentiation, the entry into the MCC cell-cycle variant, and the activation of the centriole biogenesis program.

CCNO is required for the early progression of MCC differentiation

We sought to decipher at which step of MCC differentiation CCNO is required. We performed scRNA-seq on differentiating ependymal progenitor cells harvested *in vitro* from three different *Ccno*^{KO} individuals at day *in vitro* 2 (DIV2) (see STAR Methods) and compared the cell composition with that observed in scRNA-seq from wild-type (WT) individuals (Figure S3A). In *Ccno*^{KO} mutants, cells at the mid- and late-deuterosome stages are no longer observed, indicating that the MCC cell-differentiation process is aborted early on. Consistent with this finding, a drastic reduction of terminally differentiated MCCs is observed, recapitulating immunostaining observations. By contrast and as expected, proliferating progenitors, which do not express *Ccno*, are unaffected in *Ccno*^{KO} samples (Figure S3A).

We inferred a shared differentiation lineage from co-embedded WT and *Ccno*^{KO} cells. We used it to precisely identify the lineage time point at which *Ccno*^{KO} deuterosomal cells stop differentiating (Figures S3B and S3C; STAR Methods), corresponding to a transcriptional state reached by deuterosomal cells in both WT and *Ccno*^{KO} conditions. We reannotated deuterosomal cells prior to this lineage time point as primordial deuterosomal cells (Figure 3A). In *Ccno*^{KO} primordial deuterosomal cells, the master regulator of MCC differentiation *Gmnc* is not differentially expressed, confirming that *Ccno*^{KO} cells successfully engage in the MCC fate (Figure 3B). Consistently, *Foxj1*, *Myb*, and *p73* are also not differentially expressed in *Ccno*^{KO} pri-

mordial deuterosomal cells (Figures 3B and S3D), and *FOXJ1*⁺ cells are present in comparable proportions in *in vitro* cultures of WT or *Ccno*^{KO} differentiating radial glial mouse progenitors (Figure 3C). In contrast, *Mcidas* expression is halved in *Ccno*^{KO} primordial deuterosomal cells compared to their WT counterparts (Figure 3B), contrary to what has been previously documented in mouse tracheal epithelial cells (mTECs) by bulk RT-qPCR.¹⁹ We transfected *Ccno*^{KO} cells with *Mcidas* or *Mcidas* + *Ccno* and could only restore multiciliogenesis when both factors were re-expressed, indicating that the MCC differentiation arrest in *Ccno*^{KO} is not caused by the decreased expression of *Mcidas* (Figure S3E).

To further characterize the transcriptional landscape preceding the differentiation arrest, we performed genome-wide differential expression analysis between WT and *Ccno*^{KO} primordial deuterosomal cells (Figure 3D). We identified dozens of differentially expressed genes, such as *Cdc20*, *Top2a*, *Aurka*, *Wee1*, and *Plik4* that are downregulated in *Ccno*^{KO} cells or *Cfap53*, *Pifo*, and *Spag1* genes that are upregulated in *Ccno*^{KO} cells. Using genome-wide gene set enrichment analysis (GSEA), we found that sets of genes involved in cell-cycle pathways, including cell-cycle regulation and centrosome regulation, are overall downregulated in *Ccno*^{KO} primordial deuterosomal cells. In contrast, sets of genes involved in cilia biogenesis and motility are upregulated in *Ccno*^{KO} primordial deuterosomal cells (Figure 3E). These results reveal that in the absence of *Ccno*, MCC progenitors can enter the MCC differentiation lineage and even trigger the expression of cilia biogenesis factors. However, they arrest early on in the differentiation process, concomitantly with a decreased expression of cell-cycle and centriole biogenesis factors.

Absence of CCNO blocks the progression through the MCC cell-cycle variant

Waves of canonical and non-canonical cyclins segment the MCC cell-cycle variant in successive phases, as described in

Figure 2. Cyclin O is expressed at the onset of MCC differentiation, MCC cell-cycle variant, and MCC centriole amplification

- (A) Immunostaining of ependymal cells in culture at day *in vitro* 5 (DIV5) for FOP (centrioles), GT335 (cilia), and CCNO. CCNO staining is shown for the main stages of centriolar multiplication, from the progenitor 2-centrioles state to the fully mature multiciliated cell (MCC). Centrioles are represented by rectangles with black borders, deuterosomes by red circles, and cilia by gray lines. Scale bars, 5 μm.
- (B) Nuclear and cytoplasmic intensity quantification of CCNO staining during the different stages shown in (A), normalized to the mean of centrosome stage intensity. The violin plots represent the distribution of values; the dashed horizontal line shows the median value, and the dotted horizontal lines show the interquartile range. Bottom graph shows nuclear/cytoplasmic intensity ratio (mean ± SD) per quantified coverslip for each stage. Values from $n = 3$ independent cultures of several WT mice pooled together for each experiment. Nuclear intensity: centrosome, 470 cells; A phase, 92 cells; G phase, 59 cells; D phase, 66 cells; MCCs, 188 cells. Cytoplasmic intensity: centrosome, 269 cells; A phase, 92 cells; G phase, 58 cells; D phase, 63 cells; MCCs, 175 cells. p values are derived from Kruskal-Wallis test + Dunn's multiple comparisons, *** $p < 0.0001$.
- (C) scRNA-seq data of cultured ependymal cells at DIV2 and their cluster annotation in uniform manifold approximation and projection (UMAP), as described in Serizay et al.¹¹
- (D) UMAP of cells colored by their pseudotime from 0 (cycling progenitors) to 1 (late MCCs), with intermediate values attributed to progenitors and differentiating cells, as described in Serizay et al.¹¹
- (E) UMAP of cells colored by their putative cell-cycle phase annotations inferred from neural stem cells,²² as described in Serizay et al.¹¹
- (F) UMAP of cells colored by their *Ccno* level of expression. Expression spans early and mid deuterosomal cell clusters described in (C).
- (G) Schematic representation of the main differentiation factors and centriolar assembly proteins involved in MCC differentiation steps.
- (H) Expression of several MCC differentiation factors along differentiation pseudotime and their mean expression (black line), compared to *Ccno* expression (green thick line).
- (I) Expression of cell-cycle factors along differentiation pseudotime and their mean expression (black line) compared to *Ccno* expression (green thick line).
- (J) Expression of centriole biogenesis factors along differentiation pseudotime and their mean expression (black line) compared to *Ccno* expression (green thick line).

See also Figure S2.

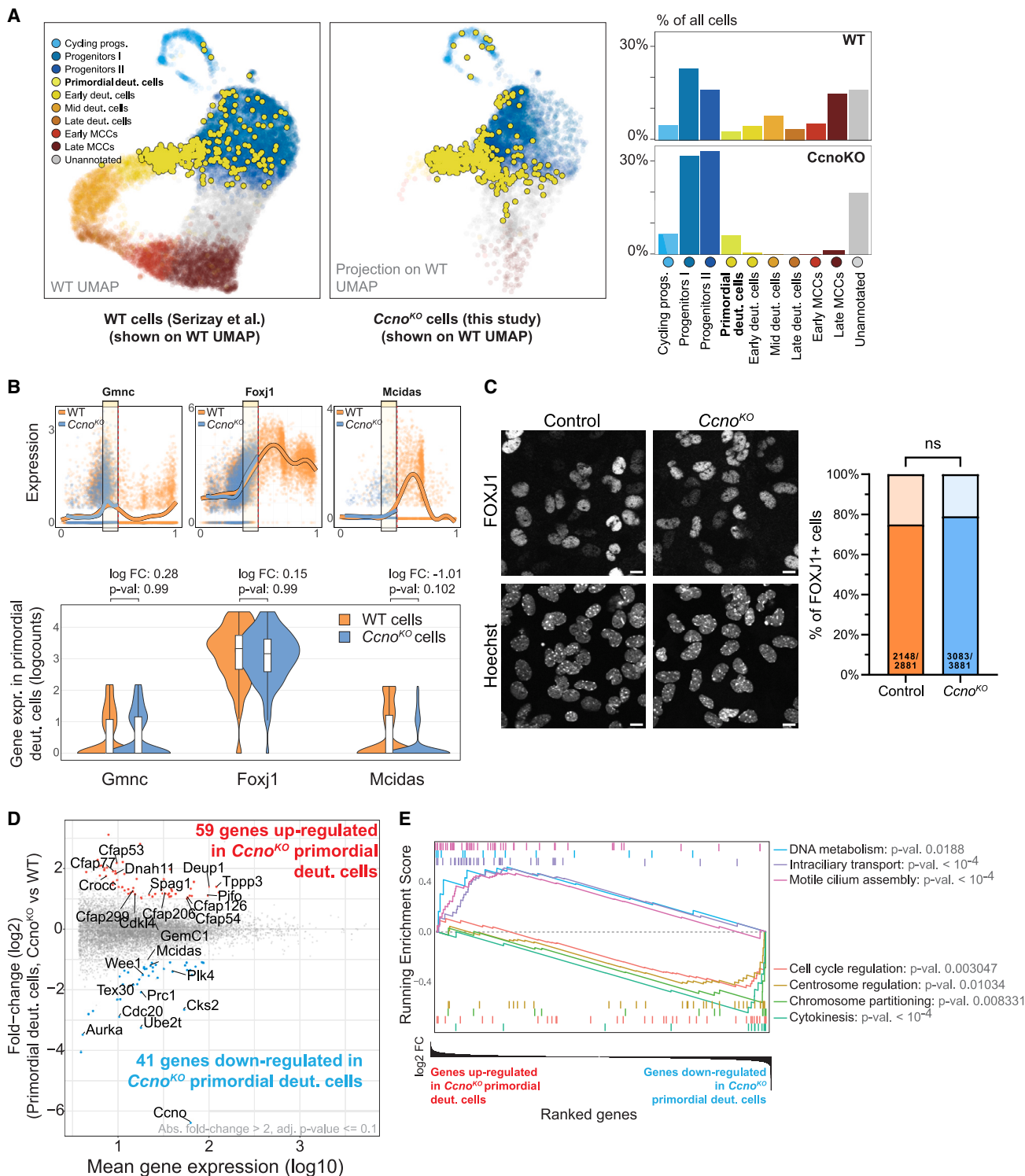


Figure 3. CCNO is required for the early progression of MCC differentiation

(A) scRNA-seq data of *Ccno*^{KO} cells compared to the previously shown dataset of WT cells (Figure 2C). *Ccno*^{KO} cells are projected onto the WT UMAP embedding, and annotations are transferred from WT to *Ccno*^{KO} cells. Note that very few cells in the deuterosomal clusters are present in the *Ccno*^{KO}. Primordial deuterosomal cell clusters, present in WT and *Ccno*^{KO} samples, are shown in yellow.

(legend continued on next page)

the companion study. CCNO is the main cyclin expressed during the first part of the MCC cell-cycle variant.¹¹ We further analyzed the *Ccno*^{KO} scRNA-seq data and found that, whereas WT deuterosomal cells can progress into S-like and G₂/M-like phases, *Ccno*^{KO} primordial deuterosomal cells arrest just before the transition into the S-like phase (Figures 4A and 4B). Consistent with CCNO being phylogenetically closer to canonical cell-cycle cyclins than to atypical cyclins (Quandt et al.²⁶; Figure S1A), this suggests that CCNO is required for the progression of progenitor cells through cell-cycle-like phases of differentiation, comparable to the role of the canonical CCNE2 for progression through the G₁/S phase of the canonical cell cycle.

To validate the role of *Ccno* for progression through successive phases of the MCC cell-cycle variant, we performed immunostaining on p27^{Kip1}, whose degradation is a hallmark of cycling cells entering S phase²⁷ and of differentiating MCCs progressing through the A, G, or D stages of centriole amplification.⁸ We quantified p27 negativity in FOXJ1⁺ WT or *Ccno*^{KO} cells. In contrast to the increasing number of FOXJ1⁺/p27⁻ cells in WT progressing into the MCC differentiation early A stage ($\approx 40\%$), we observed very few FOXJ1⁺/p27⁻ cells in FOXJ1⁺ *Ccno*^{KO} cells ($\approx 4\%$), closer to WT FOXJ1⁺ cells before centriole amplification, at the “centrosome” stage ($\approx 1\%$, Figures 4C and 4D). We also stained WT and *Ccno*^{KO} cultures for retinoblastoma protein phosphorylation (pRB pSer807/811), another hallmark of cycling cells entering S phase,²⁸ which was recently shown to also turn positive during early MCC differentiation.^{29,30} Consistent with the p27 observations, while the proportion of pRB⁺ cells begins to increase in FOXJ1⁺ WT cells entering A stage ($\approx 36\%$), very few cells are pRB⁺ in FOXJ1⁺ *Ccno*^{KO} cells ($\approx 3\%$), a proportion comparable to the proportion observed in WT FOXJ1⁺ cells at the centrosome stage ($\approx 4\%$) (Figures 4E and 4F).

Together, these results show that *Ccno*^{KO} cells can commit to becoming MCCs but stop their differentiation before p27 degradation and RB1 phosphorylation, suggesting that CCNO is necessary to enter the S-like phase of the MCC cell-cycle variant.

Absence of CCNO blocks centriole amplification at the onset of centriole biogenesis

To better characterize the differentiation arrest in *Ccno*^{KO} cells with regard to centriole biogenesis, we analyzed the expression of genes coding for (1) DEUP1, the main component of deuterosomes involved in the scaffolding of centriole biogenesis, (2) PLK4, the master regulatory kinase involved in centriole assembly, and (3) SAS6, the cartwheel protein necessary for the onset

of centriole assembly. Temporal gene-expression analysis of the scRNA-seq data show that *Deup1* is successfully activated in *Ccno*^{KO} cells at the primordial stage. *Plk4* is also activated in mutant cells, although slightly downregulated (Figure 3D), and *Sass6*, predominantly expressed after the primordial stage, remains unexpressed in *Ccno*^{KO} cells (Figure 5A). These data suggest that, at least at the transcriptional level, *Ccno*^{KO} cells can prepare for centriole amplification by expressing *Deup1* and *Plk4* early in the primordial, G₀/G₁-like phase. The arrest before the expression of *Sass6* suggests that they may not be able to progress further in the centriole biogenesis program.

To confirm whether and how the absence of CCNO blocks centriole biogenesis, we immunostained whole lateral ventricles and cultured ependymal cells for early centriole biogenesis molecular players. *Ccno*^{KO} cells can express DEUP1 and form deuterosomes *in vivo* and *in vitro* (Figures 5B, 5C, S4A, and S4B), albeit fewer and bigger (Figures 5B and 5D), suggesting they are blocked during centriole amplification. Consistent with scRNA-seq data, *Ccno*^{KO} cells also express PLK4 that can take the form of doughnuts, suggesting that PLK4 is correctly recruited by deuterosomes (Figures 5B, 5E, S4A, and S4C). However, while DEUP1⁺ cells are more numerous in *Ccno*^{KO} cells compared to the WT, the number of PLK4⁺ cells is comparable to that in the WT, suggesting that some *Ccno*^{KO} cells, blocked in amplification, fail to express, recruit, or maintain PLK4 (Figures 5C and 5E). While the early onset of amplification seems to proceed, almost no SAS6⁺ cells are observed *in vitro* or *in vivo* in *Ccno*^{KO} compared to the WT (Figures 5B, 5F, S4A, and S4D). No SAS6 is colocalized with DEUP1⁺ or PLK4⁺ structures (Figures 5B, 5G, S4A, and S4E). These observations are also applicable to *Ccno*^{RA} cultured cells (Figure S4F). Consistent with the apparent absence of SAS6⁺ procentrioles, both *Ccno*^{KO} and *Ccno*^{RA} cells lack mature centrioles (Figure S4G). Interestingly, while we previously showed that overexpression of *Mcidas* in *Ccno*^{KO} cells fails to restore multiciliation, looking at the progression of centriole amplification in this condition revealed that *Mcidas* overexpression restores the formation of A-stage SAS6⁺ procentrioles in a small subset of cells (Figure S4H), suggesting that a positive feedback mechanism exists between *Mcidas* and *Ccno*. Such a feedback mechanism could be based on the physical proximity of *Ccno* and *Mcidas* loci, whose genomic collinearity is conserved across tetrapods (Figure S1A). However, the procentrioles formed upon *Mcidas* overexpression never reach maturity, explaining the absence of multiciliation rescue (Figures S3E and S4H).

(B) Upper panels: MCC differentiation factors *Gmnc*, *Foxj1*, and *Mcidas* expression (logcounts) along MCC differentiation pseudotime from WT and *Ccno*^{KO} samples. Dots represent the level of expression in individual cells and lines represent the mean expression. Boxes outline the primordial deuterosome cell stage. Lower panel: *Gmnc* and *Foxj1* expression in primordial deuterosomal cells is similar in WT and *Ccno*^{KO}, and *Mcidas* expression is slightly downregulated in the *Ccno*^{KO} primordial cells.

(C) Left: immunostaining of FOXJ1 in *in vitro* ependymal cell cultures. Scale bars, 10 μ m. Right: quantification of the proportion of control vs. *Ccno*^{KO} FOXJ1⁺ positive cells in cultures from DIV2 to DIV23, showing that FOXJ1 expression is not affected in *Ccno*^{KO} cells at the protein level. Images from cultured cells of five control mice and eight *Ccno*^{KO} mice at the different ages mentioned were quantified. *p* values are derived from two-sided chi-squared test (two-proportion *Z* test); ns, not significant.

(D) Genome-wide differential expression analysis between WT and *Ccno*^{KO} primordial deuterosomal cell clusters, showing 59 genes upregulated and 41 genes downregulated in the *Ccno*^{KO}.

(E) GSEA of genes ranked by their expression change in *Ccno*^{KO} vs. WT primordial deuterosomal cells, showing upregulation of genes involved in cilia motility in *Ccno*^{KO} primordial cells and a downregulation of genes involved in cell cycle and centrosome regulation.

See also Figure S3.

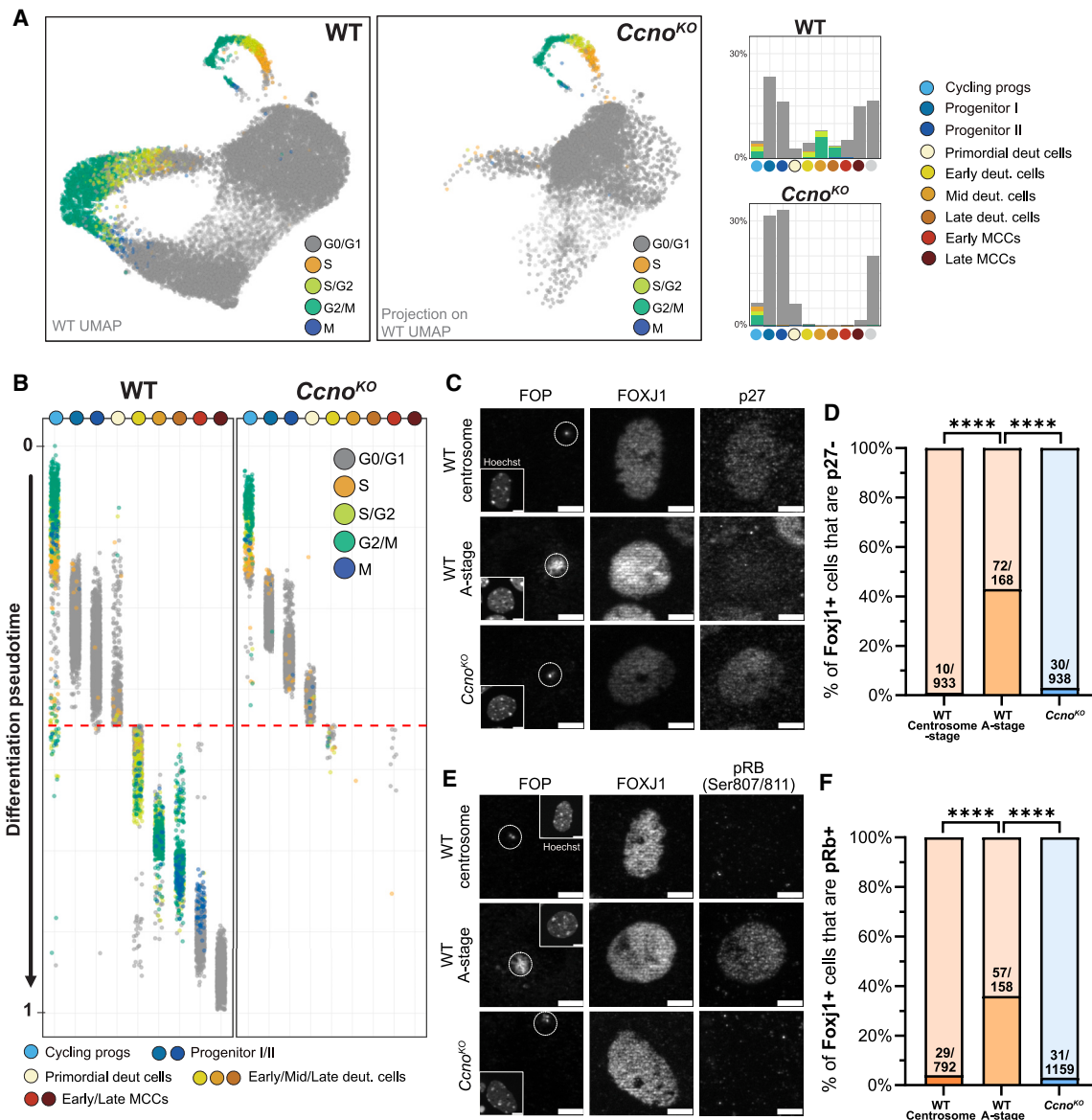


Figure 4. Absence of CCNO blocks progression through the MCC cell-cycle variant

- (A) Putative cell-cycle phase annotations of WT and *Ccno*^{KO} cells, showing a lack of S/G₂/M-like deuterosomal cells in the *Ccno*^{KO}.
- (B) Putative cell-cycle phase annotations for each cluster in WT and *Ccno*^{KO} samples along a shared differentiation pseudotime, showing that *Ccno*^{KO} are blocked at the G₀/G₁-like phase before entry into S-like phase.
- (C) Immunostaining of *in vitro* WT and *Ccno*^{KO} MCC progenitors at DIV5 for FOP, FOXJ1, and p27. Centrioles of the centrosome are FOP positive. The A stage of centriole amplification is identified by the formation of a FOP⁺ cloud. Cells with a FOP⁺ cloud are not observed in *Ccno*^{KO}. Scale bars, 5 μm.
- (D) Quantification of the percentage of p27 negative cells in FOXJ1⁺ WT centrosome-stage cells, FOXJ1⁺ WT A-stage cells, and FOXJ1⁺ *Ccno*^{KO} cells. Images from cultured cells of four control mice and four *Ccno*^{KO} mice were quantified. *p* values are derived from two-sided chi-squared test (two-proportion Z test), ****p* < 0.0001.
- (E) Same as in (C) with the immunostaining of pRB (Ser807/Ser811) along with FOP and FOXJ1. Scale bars, 5 μm.
- (F) Same as in (D) with the quantification of pRB⁺ cells. Images from cultured cells of four control mice and four *Ccno*^{KO} mice were quantified. *p* values are derived from two-sided chi-squared test (two-proportion Z test), ****p* < 0.0001.

To test the presence of procentrioles at the ultrastructural level, we used transmission electron microscopy (TEM) on cultured cells of both WT and *Ccno*^{RA} undergoing MCC differentiation. While WT cells undergoing differentiation show deuterosomes decorated with A- or G-stage procentrioles, no

procentrioles are detected on deuterosomes in *Ccno*^{RA} differentiating cells (Figures 5H and S5). In addition, and consistent with immunostaining data, deuterosomes are fewer, larger, and denser in *Ccno*^{RA} cells than in WT cells (Figures 5D, 5H, S4F, and S5).

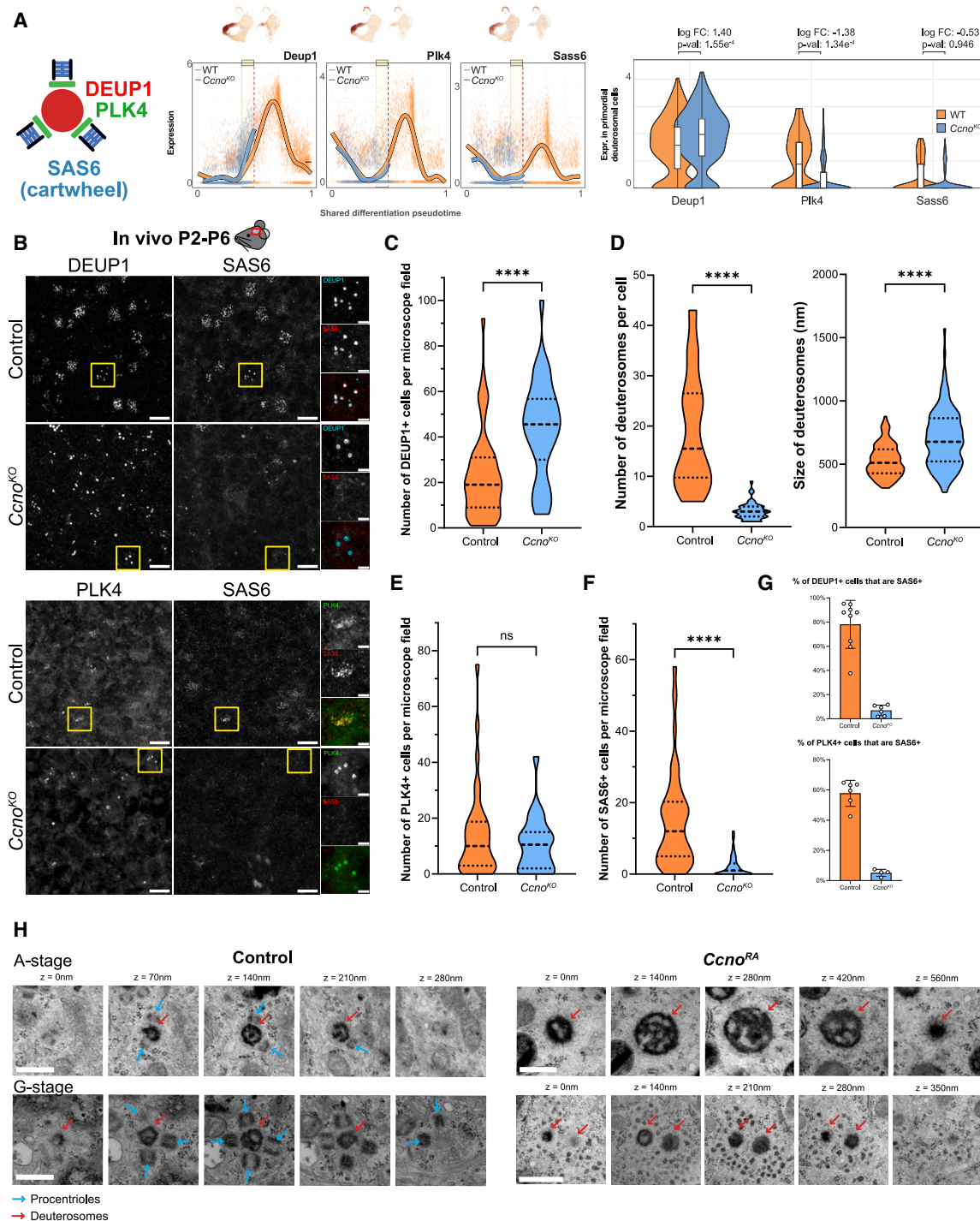


Figure 5. Absence of CCNO blocks centriole amplification at the onset of centriole biogenesis

(A) Expression levels (logcounts) of critical centriolar assembly proteins involved in centriole amplification (*Deup1*, *Plk4*, and *Sass6*) along MCC differentiation pseudotime (left) and in primordial deuterosomal cells (right) in WT and *Ccno*^{KO} scRNA-seq datasets. Boxes in left panels outline the primordial deuterosome cell stage along the differentiation pseudotime.

(B) Immunostaining of whole-mount lateral ventricles of mice pups aged P2–P6 for DEUP1, PLK4, and SAS6. Scale bars, 10 μm for large-field images and 2.5 μm for zoom-ins.

(C) Quantification of the number of DEUP1+ cells in microscope field in control and *Ccno*^{KO}, showing that *Ccno*^{KO} have more cells that express DEUP1 compared to the control. Images from nine control mice and six *Ccno*^{KO} mice were quantified, with six images per immunostained tissue. Control, 54 values; *Ccno*^{KO},

(legend continued on next page)

Taken together, these results show that mouse brain cells lacking CCNO cannot form the future basal bodies necessary for multiple cilia formation because of a block in centriole amplification at the very early onset of centriole assembly, due to a stop before SAS6 expression.

Human airway MCC phenotype in the absence of CCNO is similar to that of mouse brain MCCs

CCNO was the first gene found to be mutated¹⁸ in a human condition heterogeneously named “acilia syndrome,” “ciliary aplasia,” or “oligocilia phenotype,” and grouping human patients with seemingly bald respiratory epithelia and presenting symptoms similar to those of PCD.^{31–44} Although patients with RGMC present a higher rate of hydrocephalus compared to the general population, the most debilitating phenotype remains chronic airway infections. The cell-cycle variant identified in mouse brain cells seems to be conserved in mouse and human respiratory cells.^{11,12} To characterize the role of CCNO in human airway epithelial cells and test whether it is more akin to mouse brain or airways, we generated an hESC H9 line with a 14-bp homozygous deletion in the CCNO gene (hereafter referred to as CCNO^{−/−}), which produces a truncated protein product (Figures S6A–S6D). Mutation of the CCNO gene did not appear to affect the pluripotency or genetic stability of H9 cells (Figures S6E–S6H). WT and CCNO^{−/−} H9 cells were differentiated into airway epithelial cells following a directed differentiation protocol that was adapted.^{45,46} No significant differences were observed in the ability of WT and CCNO^{−/−} H9 cells to differentiate into lung progenitors and airway basal cells (Figures S7A–S7C). We then immunostained WT and CCNO^{−/−} hESC-derived airway epithelial cells cultured under air-liquid interface (ALI) conditions for MCC differentiation (FOXJ1, RFX2, RFX3), procentriole (SAS6), and cilia (GT335) markers (Figures 6A–6E and S7D). This reveals that, while WT and CCNO^{−/−} cells can both acquire MCC fate as shown by FOXJ1, RFX2, and RFX3 positivity, only WT cells can produce SAS6⁺ procentrioles and grow multiple cilia (Figures 6B–6F and S7D), suggesting that, in the absence of CCNO, human airway epithelial cells encounter a block in their differentiation at the early onset of centriole biogenesis, as also found in the mouse brain.

To confirm this finding, we analyzed nasal brushing biopsies from 15 different patients with mutations in the CCNO gene by

TEM (Tables S1 and S2). Previous studies on respiratory MCCs from patients with CCNO mutations mainly reported cilia scarcity and difficulties in finding basal bodies by electron microscopy.^{13,14,16,18} However, the absence of quantification has left unclear whether the phenotype is severe, as in the *Ccno* mutant mouse brain, or milder, as in its trachea. To identify differentiated cells in patients, we focused our analysis on cells with microvilli, a feature of MCC differentiation. We found that while 94% of cells (305/324) from patients from the control group present multiple basal bodies, almost no patients with CCNO mutations have cells in TEM sections (0.1%; 5/420) that show more than two centrioles, suggesting that they fail to amplify centrioles and form basal bodies. In line with this, in contrast to control patients' cells, patients with CCNO mutations' cells do not form multiple cilia (Figures 6G, 6H, and S8A). The three CCNO mutated cells presenting few basal bodies and cilia come from patient H (Figures 6H and S8B), who carries the frameshift pathogenic variation c.793dup p.(Val265Glyfs*106) on one allele, resulting in a premature stop codon in the last exon. Transcripts from this allele likely escape nonsense-mediated mRNA decay and may underlie the production of a potentially hypomorphic protein that retains the first cyclin domain. Interestingly, in a subset of cells coming from the 15 patients with CCNO mutations, TEM sections reveal centriolar attributes such as electron-dense aggregates, which are centriolar satellites known to be involved in centriole or cilia formation^{47–49} (Figures 6G [top zoom-ins], 6I, and S13A), and rootlets, which constitute the roots of mature centrioles (Figures 6G [top zoom-ins], 6J, and S8A). This is consistent with scRNA-seq of mouse *Ccno*^{KO} cells showing that mRNA levels of *Pcm1* (coding for the core component of centriolar satellites) and *Crocc1* (coding for the protein Rootletin, core component of the rootlet) are not changed or are upregulated, respectively, in deuterosomal primordial cells (Figure 3D). This suggests that, as in mouse brain cells, the CCNO mutant human airway MCCs prepared for centriole amplification but were interrupted in the process.

Altogether, these observations suggest that human respiratory MCCs need CCNO to enter the cell-cycle variant and produce centrioles as do mouse brain MCCs, and that patients can present mutations leading to the production of a hypomorphic protein that can facilitate the biogenesis of few basal bodies or cilia.

36 values. *p* values are derived from two-tailed Mann-Whitney U test, ****p* < 0.0001. The distribution is represented with violin plots, the dashed horizontal line showing the median value and the dotted horizontal lines showing the interquartile range.

(D) Quantification of the number of deuterosomes per cell (left) and size of deuterosomes (right) between control and *Ccno*^{KO}. Deuterosomes from three control mice and three *Ccno*^{KO} mice were counted and measured, randomly chosen from the previously quantified dataset for DEUP1⁺ cells. Number of deuterosomes: control, 30 values; *Ccno*^{KO}, 52 values. Size of deuterosomes: control, 144 values; *Ccno*^{KO}, 128 values. *p* values are derived from two-tailed Mann-Whitney U test, ****p* < 0.0001. Data are presented as in (C).

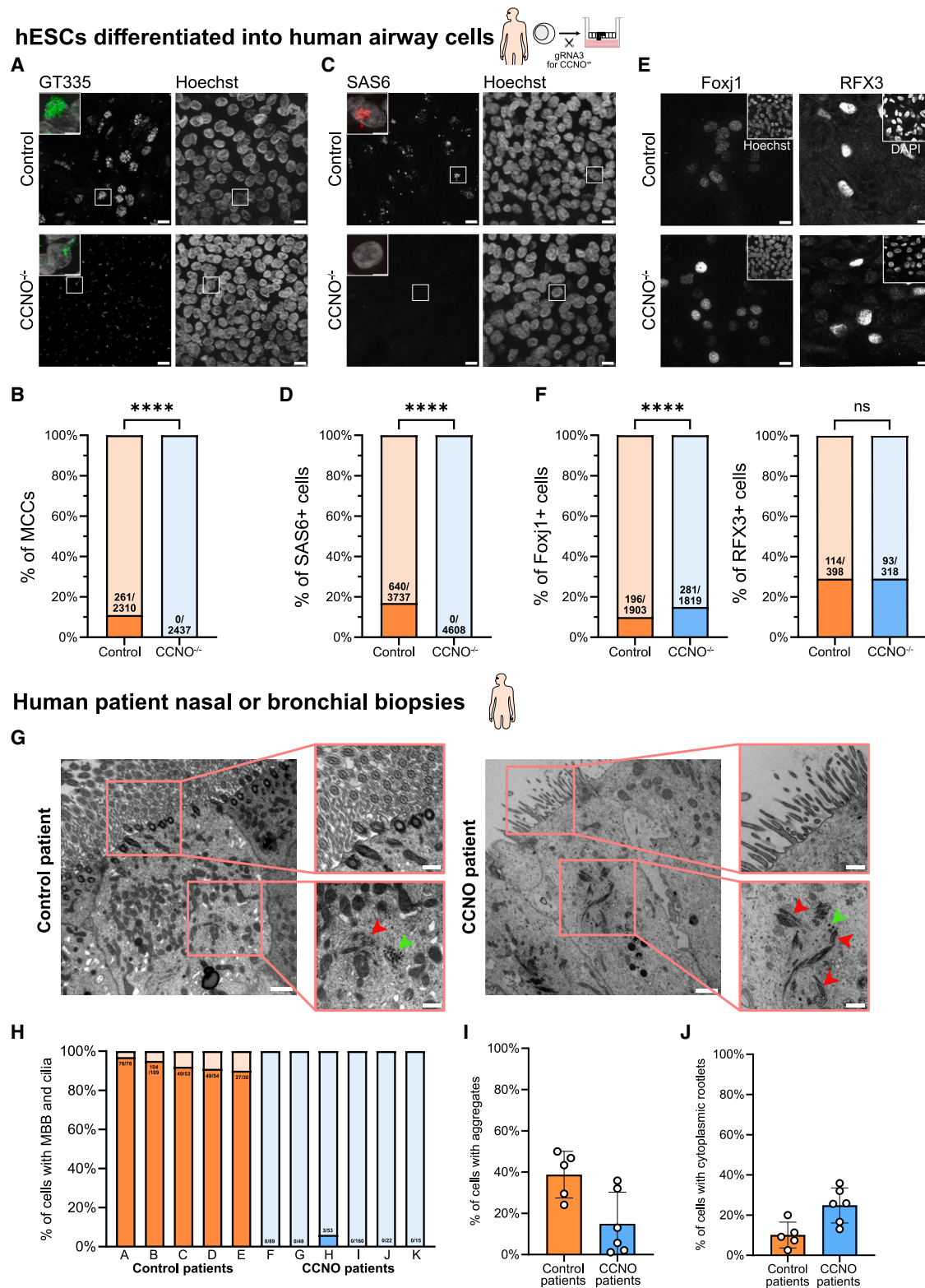
(E) Quantification of the number of PLK4⁺ cells per microscope field in control and *Ccno*^{KO}. Images from six control mice and four *Ccno*^{KO} mice were quantified, with six images per immunostained tissue. Control, 36 values; *Ccno*^{KO}, 24 values. *p* values derived from two-tailed Mann-Whitney U test; ns, not significant. Data are presented as in (C).

(F) Quantification of the number of SAS6⁺ cells per microscope field in control and *Ccno*^{KO}. Images from nine control mice and six *Ccno*^{KO} mice that were previously used for either PLK4 or DEUP1 quantification were quantified, with six images per immunostained tissue. Control, 90 values; *Ccno*^{KO}, 60 values. *p* values are derived from two-tailed Mann-Whitney U test, ****p* < 0.0001. Data are presented as in (C).

(G) Quantification of the proportion of DEUP1⁺ cells and PLK4⁺ cells that can express SAS6 in both control and *Ccno*^{KO}. One point represents an animal, quantified from the same images used to quantify DEUP1⁺, PLK4⁺, and SAS6⁺ cells. Columns represent the average quantification, and error bars represent SD.

(H) Serial electron microscopy ultra-thin sections of control and *Ccno*^{RA} cells *in vitro* at DIV5. Control cells show deuterosomes decorated with either A- or G-stage procentrioles. Deuterosomes are indicated by red arrows. Blue arrows indicate procentrioles in the control. Scale bars, 0.5 μm.

See also Figures S4 and S5.



(legend on next page)

DISCUSSION

This study shows that CCNO controls the entry into the MCC cell-cycle variant (described in a companion study by Serizay et al.¹¹) and the subsequent centriole amplification required for multiple cilia formation (Figure 7). This work and the associated study¹¹ argue in favor of CCNO acting as a canonical cyclin, involved in switch-like transitions of a cell-cycle variant rather than an atypical cyclin. First, *Ccno* is one of the four cyclins expressed as successive waves along the MCC cycle variant, between *Ccnd2* and *Ccnb1/Ccna1*, and its expression is temporally correlated with *Ccne2* along the canonical cell cycle. Consistently, the expression of *Ccno* covers the expression of S-phase and G₂/M-transition regulators. Second, CCNO depletion leads to the lack of nearly all cells annotated for post-G₀/G₁ cell-cycle-like phases or positivity for hallmarks of cell-cycle entry and progression (e.g., RB phosphorylation and p27 degradation). Finally, we show that *Ccno* is also expressed as a comparable wave, associated with the silencing of *Ccne* and the subsequent expression of *Ccnb1* and *Ccna1*, during male meiosis.¹¹ *Ccno* is also expressed during female oogenesis, where it is involved in meiotic progression.⁵⁰ Altogether, these observations strongly support the role of CCNO as a canonical cyclin involved in the entry and progression of non-traditional cell-cycle variants, characterized by the production of centrioles uncoupled from DNA replication.

The earliest steps of centriole biogenesis during the canonical cell cycle occur at the G₁/S transition, concomitant with DNA replication.⁵¹ Yet how and with which temporality the transcription of genes coding for centriole components are regulated is obscure, probably because only two centrioles are produced and transcripts are challenging to detect. During massive amplification of centrioles in MCCs and with single-cell transcriptomic resolution, we uncover a transcriptional cascade of core centriole regulators, where centriole scaffolding components *Deup1*, *Cep152*, and *Plk4* expression onsets slightly precede early centriolar components such as *Sass6* and *Stil*, which precede centriole maturation core regulators such as *Poc5*, *Ninein*, and *Cep164*. The expression of some of the genes coding for motile cilia components occurs later (Figures 2G, 2H, and S2C). Interestingly, the block in differentiation characterized in the *Ccno*^{KO} mutant, which occurs before the entry into the S-like phase, follows the onset of expression of centriole scaf-

folding components and precedes the activation of genes coding for core centriole constituents, from the earliest one, SAS6. This leads to the production of deuterosomes decorated with PLK4 but to the lack of procentrioles, basal bodies, and cilia. Supporting the proximity in regulating meiosis and MCC differentiation by CCNO, the block under CCNO depletion is associated with a block in microtubule-organizing center formation during mouse female meiosis (spindle poles are acentriolar in female meiosis⁵⁰). Altogether, our data show that the coupling of centriole biogenesis to an S-like phase entry in the MCC cell-cycle variant is maintained, as previously suggested by the involvement of MYB in centriole amplification^{52,53}—although DNA does not replicate—and is dependent on CCNO.

In contrast to mouse brain and human airways, in mouse airways and oviducts, CCNO depletion authorizes the formation of around 30% of MCCs (Funk et al.¹⁹; Núñez-Ollé et al.²⁰; this study). Yet most of these cells display abnormal ciliation, which suggests that they most likely compensate for the loss of CCNO rather than belonging to a different population, differentiating through a CCNO-independent pathway. Functional redundancy and compensation for chronic depletion of cyclins or CDKs have been known for a long time.⁵⁴ Consistent with a possible rescue by another cyclin, CCNO probably acts through canonical CDK activation in MCCs, since it binds and activates CDK1 and CDK2 when ectopically expressed in HEK293 cells⁵⁵ and acts through the binding with CDK1 or CDK2 during meiosis and apoptosis, respectively.^{50,55} In addition, we fail to rescue CCNO depletion by expressing a CDK-dead version of CCNO in brain MCCs (Figures S9A and S9B). Interestingly, we observed that while E-type cyclins are not expressed in both mouse brain and human respiratory cells (*in vitro* and *in vivo*), *Ccne1* is significantly re-expressed in deuterosomal cells in mouse respiratory tract (*in vitro* data from Ruiz-Garcia et al.⁵⁶ and Choksi et al.¹²; Figure S9C). This difference suggests that CCNE1 could compensate CCNO absence in respiratory tissues and partially support multiciliation. In addition, this population of cells escaping the most severe phenotype shows later defects, revealing a role for CCNO during the late stages of centriole amplification,¹⁹ consistent with the expression of CCNO during the G stage of centriole biogenesis and G₂/M-like stages of the MCC cell-cycle variant. Since normal ciliation seems also possible in mutant tissues, it suggests that even the later role of CCNO in centriole maturation and subsequent ciliation can

Figure 6. Human airway phenotype in the absence of CCNO is similar to that of mouse brain MCCs

(A and B) (A) Immunostaining of hESCs control or expressing non-functional CCNO (CCNO^{-/-}) and differentiated into human epithelial airway cells with GT335 and (B) quantification of multiciliated cells. Scale bars, 10 μm for large-field images and 5 μm for zoom-ins. *p* values are derived from two-sided chi-squared test (two-proportion Z test), ****p* < 0.0001.

(C and D) (C) Immunostaining of the same cells as previously with SAS6 and (D) quantification of SAS6⁺ cells. Scale bars, 10 μm for large-field images and 5 μm for zoom-ins. *p* values are derived from two-sided chi-squared test (two-proportion Z test), ****p* < 0.0001.

(E and F) (E) Immunostaining of the same cells as previously with FOXJ1 and RFX3 and (F) quantification of FOXJ1⁺ and RFX3⁺ cells. Scale bars, 10 μm. *p* values are derived from two-sided chi-squared test (two-proportion Z test), ****p* < 0.0001; ns, not significant.

(G) Airway epithelium of control and patients with CCNO mutations under TEM. Scale bars, 1 μm for large-field images and 0.5 μm for zoom-ins.

(H) Quantification of the number of cells with microvilli that have more than 2 basal bodies (MBB) and/or cilia in patients from the control group and patients with CCNO mutations, with examples shown in the top zoom-in pictures of (G).

(I and J) Quantification of cells with microvilli in human control and patients with CCNO mutations showing the presence of centriolar aggregates (green arrowheads) and cytoplasmic rootlets (red arrowheads) indicated in the bottom zoom-in pictures in (G). Columns represent the average quantification, and error bars represent SD.

See also Figures S6–S8; Tables S1 and S2.

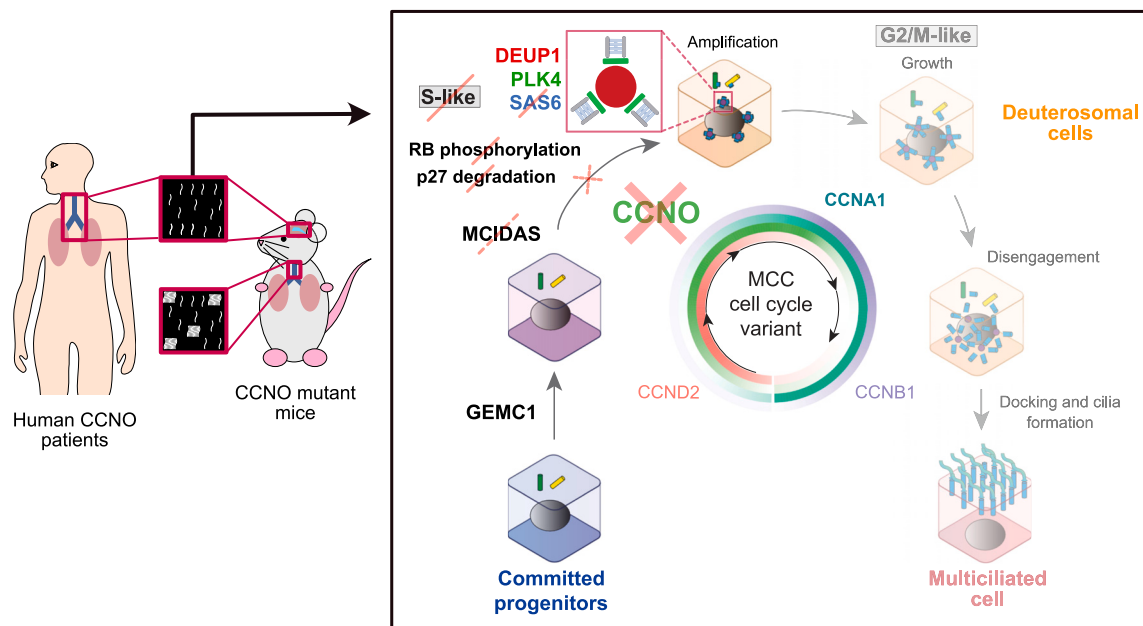


Figure 7. Cyclin O is necessary for multiciliated cells to enter their differentiation cell-cycle variant and allows the massive amplification of centrioles, which serve as basal bodies for cilia nucleation

See also Figure S9.

be compensated. The analysis of the expression of canonical and non-canonical cyclins, Cdks, APC/C inhibitors, E2fs, and key differentiation factors *Mcidas* and *Gmnc* in different populations in mouse brain or human/mouse respiratory MCCs did not reveal other striking differences that could explain this differential phenotype (Figure S9C).

Ccno is part of a locus containing two other genes involved in multiciliation (*Mcidas* and *Cdc20b*⁵⁷). Interestingly, their clustering, order, and collinearity are conserved among tetrapods, and the temporality of their expression along the pseudotime of differentiation follows their order along the DNA strand, with *Mcidas* and *Ccno* quasi-simultaneously expressed in brain MCCs (Figure S2D). This conserved collinearity could play a role in the successive activation of each gene through the spreading of local chromatin remodeling. Using single-cell resolution transcriptomic measurements, we consistently show that *Ccno* depletion leads to decreased *Mcidas* expression. Nonetheless, it has been demonstrated in other studies that *Mcidas* depletion also blocks *Ccno* expression.^{18,58,59} We therefore propose a positive feedback loop between *Mcidas* and *Ccno* whereby *Mcidas* activates *Ccno* expression, which in turn activates *Mcidas* expression. Consistent with this hypothesis, *Mcidas* depletion leads to a phenotype comparable to that of *Ccno* mutant,^{58–60} overexpression of *Mcidas* in *Ccno*-depleted cells rescues early amplification in a subset of mouse brain cells (this study), and *Mcidas* depletion is not compensated in mouse airways.⁵⁹ Such a positive feedback loop would be reminiscent of G₁ cyclins, which increase their transcription to increase cyclin-CDK activity, ensuring commitment to the cell cycle and activation of the entire G₁/S transcriptional network.⁶¹

Altogether, our study identifies (1) CCNO as the core regulator of entry into the MCC cell-cycle variant and (2) the interruption of this new variant as one etiology of RGMC. Future work is now needed to identify the CDK partner of CCNO.

Limitations of the study

In this paper we focus on the role of CCNO in the new MCC cell-cycle variant in the mouse brain MCC model. We demonstrate that human respiratory cells show the same phenotype as mouse brain cells. While some mouse respiratory cells can compensate for the loss of CCNO, we do not identify the molecular mechanism of this compensation. Most importantly, future work is needed to identify the CDK binding partner for CCNO and their specific substrates. This would greatly enhance our understanding of the mechanisms by which the canonical cell cycle is deviated to drive a strict cytoplasmic centriole amplification process. Also, we provide evidence that MCIDAS and CCNO could form a positive feedback loop, but the specificities of this regulation are not resolved.

RESOURCE AVAILABILITY

Lead contact

Further information and requests for resources and reagents should be directed to and will be provided by the lead contact, Alice Meunier (alice.meunier@bio.ens.psl.eu).

Materials availability

This paper did not generate new unique reagents.

Data and code availability

- Raw and processed sequencing data have been deposited at the NCBI Gene Expression Omnibus (<https://www.ncbi.nlm.nih.gov/geo/>) under the accession GEO: GSE201773 and are publicly available as of the

date of publication. Processed scRNA-seq data are also available for interactive investigation using cellxgene (collection #33f48a52-31d8-4cc8-bd00-1e89c659a87f) at <https://cellxgene.cziscience.com/collections/33f48a52-31d8-4cc8-bd00-1e89c659a87f> as of the date of publication. Accession numbers are also listed in the [key resources table](#).

- All original code has been deposited at Zenodo (record #14105247) and is publicly available at <https://doi.org/10.5281/zenodo.14105247> as of the date of publication. The Zenodo accession number is also listed in the [key resources table](#).
- Any additional information required to reanalyze the data reported in this paper is available through the [lead contact](#) upon request.

ACKNOWLEDGMENTS

We thank all members of the Spassky lab who contributed to the elaboration of this research work. We also thank the IBENS administrative team and imaging platform for their support and the IBENS Animal Facility for animal care. We thank Kévin Lebrigand and Virginie Magnone for fruitful discussions on scRNA-seq. We thank Xavier Morin and Stavros Taraviras for sharing plasmids. This work is supported by funding to A.M. from the ANR (ANR-19-CE13-0027) and Q-life Program. The Spassky lab is also funded by Inserm, the CNRS, the École Normale Supérieure, the ANR (ANR-20-CE45-0019, ANR-21-CE16-0016, ANR-22-CE16-0011), the European Research Council (ERC grant agreement 647466), and the Fondation pour la Recherche Médicale (FRM, EQU 202103012767). The Roy lab is supported by the Agency for Science, Technology and Research (A*STAR) and a National Medical Research Council of Singapore grant (OFIRG19nov-0037). R.K. is supported by the Institut Pasteur, CNRS, and the European Research Council (ERC grant agreement 771813); J.S. is funded by the Association pour la Recherche sur le Cancer; M.K.D. is funded by the FRM; A.-R.B. is funded by La Ligue Contre Le Cancer; C.T.J. was supported by an A*STAR Research Attachment Program (ARAP) fellowship; and S.J.A. is supported by the German Research Foundation through a Heisenberg Professorship (AR 732/3-1), project P7 of SFB 1453 (project ID 431984000) and Germany's Excellence Strategy (CIBSS – EXC-2189 – Project ID 390939984). This work was performed with support from the National Infrastructure France Génomique (Commissariat aux Grands Investissements, ANR-10-INBS-09-03, ANR-10-INBS-09-02), the 3IA Côte d'Azur (ANR-19-P3IA-0002), European Union's H2020 Research and Innovation Program under grant agreement no. 874656 (discovAIR), and Conseil départemental 06 (2016-294DGADSH-CV).

AUTHOR CONTRIBUTIONS

Conceptualization, M.K.D., J.S., and A.M.; mouse mutant generation, S.J.A. and G.G.-G.; methodology/mouse, M.K.D., J.S., A.-R.B., R.B., M.F., N.D., and L.-E.Z.; single-cell formal analysis, J.S.; methodology/human patients, M.L., C.F., E.E., R.M., D.C.B., and H.O.; methodology/hESC-derived MCCs, K.J.G., H.L., E.K.T., C.T.J., C.D.B., N.R.D., M.K.D., and S.R.; investigation, M.K.D., J.S., L.-E.Z., P.B., G.G.-G., M.L., K.J.G., H.L., E.E., H.O., D.C.B., S.J.A., R.K., S.R., N.S., and A.M.; supervision, A.M.; writing – original draft, M.K.D., J.S., and A.M.; writing – review & editing, all authors.

DECLARATION OF INTERESTS

The authors declare no competing interests.

STAR METHODS

Detailed methods are provided in the online version of this paper and include the following:

- [KEY RESOURCES TABLE](#)
- [EXPERIMENTAL MODEL AND STUDY PARTICIPANT DETAILS](#)
 - Transgenic mice
 - Human embryonic stem cell (hESC) culture
 - Human patients
- [METHOD DETAILS](#)

- Primary brain ependymal cell cultures and transfections
- Immunostainings
- Microscopy
- Single-cell RNA-seq of *in vitro* differentiating multiciliated cells
- Computational analysis of single-cell RNA-seq data
- Generation of human epithelial airway cells from human embryonic stem cell (hESC)
- Transmission electron microscopy on human respiratory cells

● QUANTIFICATION AND STATISTICAL ANALYSIS

● ADDITIONAL RESOURCES

SUPPLEMENTAL INFORMATION

Supplemental information can be found online at <https://doi.org/10.1016/j.celrep.2024.115117>.

Received: August 28, 2024

Revised: November 21, 2024

Accepted: December 5, 2024

Published: December 30, 2024

REFERENCES

1. Aprea, I., Nöthe-Menchen, T., Dougherty, G.W., Raidt, J., Loges, N.T., Kaiser, T., Wallmeier, J., Olbrich, H., Strünker, T., Kliesch, S., et al. (2021). Motility of Efferent Duct Cilia Aids Passage of Sperm Cells through the Male Reproductive System. *Mol. Hum. Reprod.* 27, gaab009. <https://doi.org/10.1093/molehr/gaab009>.
2. Spassky, N., and Meunier, A. (2017). The Development and Functions of Multiciliated Epithelia. *Nat. Rev. Mol. Cell Biol.* 18, 423–436. <https://doi.org/10.1038/nrm.2017.21>.
3. Terré, B., Lewis, M., Gil-Gómez, G., Han, Z., Lu, H., Aguilera, M., Prats, N., Roy, S., Zhao, H., and Stracker, T.H. (2019). Defects in Efferent Duct Multiciliogenesis Underlie Male Infertility in GEMC1-MCIDAS- or CCNO-Deficient Mice. *Development* 146, 162628. <https://doi.org/10.1242/dev.162628>.
4. Yuan, S., Liu, Y., Peng, H., Tang, C., Hennig, G.W., Wang, Z., Wang, L., Yu, T., Klukovich, R., Zhang, Y., et al. (2019). Motile Cilia of the Male Reproductive System Require miR-34/miR-449 for Development and Function to Generate Luminal Turbulence. *Proc. Natl. Acad. Sci. USA* 116, 3584–3593. <https://doi.org/10.1073/pnas.1817018116>.
5. LoMastro, G.M., Drown, C.G., Maryniak, A.L., Jewett, C.E., Strong, M.A., and Holland, A.J. (2022). PLK4 Drives Centriole Amplification and Apical Surface Area Expansion in Multiciliated Cells. *eLife* 11, e80643. <https://doi.org/10.7554/eLife.80643>.
6. Vladar, E.K., and Stearns, T. (2007). Molecular Characterization of Centriole Assembly in Ciliated Epithelial Cells. *J. Cell Biol.* 178, 31–42. <https://doi.org/10.1083/jcb.200703064>.
7. Zhao, H., Zhu, L., Zhu, Y., Cao, J., Li, S., Huang, Q., Xu, T., Huang, X., Yan, X., and Zhu, X. (2013). The Cep63 Parologue Deup1 Enables Massive de Novo Centriole Biogenesis for Vertebrate Multiciliogenesis. *Nat. Cell Biol.* 15, 1434–1444. <https://doi.org/10.1038/ncb2880>.
8. Al Jord, A., Shihavuddin, A., Servignat d'Aout, R., Faucourt, M., Genovesio, A., Karaiskou, A., Sobczak-Thépot, J., Spassky, N., and Meunier, A. (2017). Calibrated Mitotic Oscillator Drives Motile Ciliogenesis. *Science* 358, 803–806. <https://doi.org/10.1126/science.aan8311>.
9. Kim, S., Chien, Y.-H., Ryan, A., and Kintner, C. (2022). Emi2 Enables Centriole Amplification during Multiciliated Cell Differentiation. *Sci. Adv.* 8, eabm7538. <https://doi.org/10.1126/sciadv.abm7538>.
10. Vladar, E.K., Stratton, M.B., Saal, M.L., Salazar-De Simone, G., Wang, X., Wolgemuth, D., Stearns, T., and Axelrod, J.D. (2018). Cyclin-Dependent Kinase Control of Motile Ciliogenesis. *eLife* 7, e36375. <https://doi.org/10.7554/eLife.36375>.

11. Serizay, J., Khouri Damaa, M., Boudjema, A.-R., Faucourt, M., Delgehyr, N., Noûs, C., Zaragozi, L.-E., Barbry, P., Spassky, N., Koszul, R., and Meunier, A. (2024). Cyclin Replacement Hijacks the Cell Cycle's Genetic Regulatory Program to Orchestrate Multiciliogenesis. *Cell Rep.* **44**, 115103.
12. Choksi, S.P., Byrnes, L.E., Konjikusic, M.J., Tsai, B.W.H., Deleon, R., Lu, Q., Westlake, C.J., and Reiter, J.F. (2024). An Alternative Cell Cycle Coordinates Multiciliated Cell Differentiation. *Nature* **630**, 214–221. <https://doi.org/10.1038/s41586-024-07476-z>.
13. Amirav, I., Wallmeier, J., Loges, N.T., Menchen, T., Pennekamp, P., Mus-saffi, H., Abitbul, R., Avital, A., Bentur, L., Dougherty, G.W., et al. (2016). Systematic Analysis of CCNO Variants in a Defined Population: Implications for Clinical Phenotype and Differential Diagnosis. *Hum. Mutat.* **37**, 396–405. <https://doi.org/10.1002/humu.22957>.
14. Casey, J.P., McGettigan, P.A., Healy, F., Hogg, C., Reynolds, A., Kennedy, B.N., Ennis, S., Slattery, D., and Lynch, S.A. (2015). Unexpected Genetic Heterogeneity for Primary Ciliary Dyskinesia in the Irish Traveller Population. *Eur. J. Hum. Genet.* **23**, 210–217. <https://doi.org/10.1038/ejhg.2014.79>.
15. Guo, Z., Chen, W., Wang, L., and Qian, L. (2020). Clinical and Genetic Spectrum of Children with Primary Ciliary Dyskinesia in China. *J. Pediatr.* **225**, 157–165.e5. <https://doi.org/10.1016/j.jpeds.2020.05.052>.
16. Henriques, A.R., Constant, C., Descalço, A., Pinto, A., Moura Nunes, J., Sampaio, P., Lopes, S.S., Pereira, L., and Bandeira, T. (2021). Primary Ciliary Dyskinesia Due to CCNO Mutations—A Genotype-Phenotype Correlation Contribution. *Pediatr. Pulmonol.* **56**, 2776–2779. <https://doi.org/10.1002/ppul.25440>.
17. Ma, C., Wu, H., Zhu, D., Wang, Y., Shen, Q., Cheng, H., Zhang, J., Geng, H., Liu, Y., He, X., et al. (2021). Bi-Allelic Mutations in MCIDAS and CCNO Cause Human Infertility Associated with Abnormal Gamete Transport. *Clin. Genet.* **100**, 731–742. <https://doi.org/10.1111/cge.14067>.
18. Wallmeier, J., Al-Mutairi, D.A., Chen, C.-T., Loges, N.T., Pennekamp, P., Menchen, T., Ma, L., Shamseldin, H.E., Olbrich, H., Dougherty, G.W., et al. (2014). Mutations in CCNO Result in Congenital Mucociliary Clearance Disorder with Reduced Generation of Multiple Motile Cilia. *Nat. Genet.* **46**, 646–651. <https://doi.org/10.1038/ng.2961>.
19. Funk, M.C., Bera, A.N., Menchen, T., Kuales, G., Thriene, K., Lienkamp, S.S., Dengjel, J., Omran, H., Frank, M., and Arnold, S.J. (2015). Cyclin O (Ccno) Functions during Deuterosome-Mediated Centriole Amplification of Multiciliated Cells. *EMBO J.* **34**, 1078–1089. <https://doi.org/10.15252/embj.201490805>.
20. Núñez-Ollé, M., Jung, C., Terré, B., Balsiger, N.A., Plata, C., Roset, R., Pardo-Pastor, C., Garrido, M., Rojas, S., Alameda, F., et al. (2017). Constitutive Cyclin O Deficiency Results in Penetrant Hydrocephalus, Impaired Growth and Infertility. *Oncotarget* **8**, 99261–99273. <https://doi.org/10.18632/oncotarget.21818>.
21. Defosset, A., Merlat, D., Poidevin, L., Nevers, Y., Kress, A., Poch, O., and Lecompte, O. (2021). Novel Approach Combining Transcriptional and Evolutionary Signatures to Identify New Multiciliation Genes. *Genes* **12**, 1452. <https://doi.org/10.3390/genes12091452>.
22. O'Connor, S.A., Feldman, H.M., Arora, S., Hoellerbauer, P., Toledo, C.M., Corrin, P., Carter, L., Kufeld, M., Boulouri, H., Basom, R., et al. (2021). Neural G0: A Quiescent-like State Found in Neuroepithelial-derived Cells and Glioma. *Mol. Syst. Biol.* **17**, e9522. <https://doi.org/10.15252/msb.20209522>.
23. Lewis, M., and Stracker, T.H. (2021). Transcriptional Regulation of Multiciliated Cell Differentiation. *Semin. Cell Dev. Biol.* **110**, 51–60. <https://doi.org/10.1016/j.semcdb.2020.04.007>.
24. Lyu, Q., Li, Q., Zhou, J., and Zhao, H. (2024). Formation and Function of Multiciliated Cells. *J. Cell Biol.* **223**, e202307150. <https://doi.org/10.1083/jcb.202307150>.
25. Pan, J.-H., Adair-Kirk, T.L., Patel, A.C., Huang, T., Yozamp, N.S., Xu, J., Reddy, E.P., Byers, D.E., Pierce, R.A., Holtzman, M.J., and Brody, S.L. (2014). Myb Permits Multilineage Airway Epithelial Cell Differentiation: Myb Permits Airway Epithelial Differentiation. *Stem Cell.* **32**, 3245–3256. <https://doi.org/10.1002/stem.1814>.
26. Quandt, E., Ribeiro, M.P.C., and Clotet, J. (2020). Atypical Cyclins: The Extended Family Portrait. *Cell. Mol. Life Sci.* **77**, 231–242. <https://doi.org/10.1007/s00018-019-03262-7>.
27. Coats, S., Flanagan, W.M., Nourse, J., and Roberts, J.M. (1996). Requirement of p27Kip1 for Restriction Point Control of the Fibroblast Cell Cycle. *Science* **272**, 877–880. <https://doi.org/10.1126/science.272.5263.877>.
28. Zhou, L., Ng, D.S.-C., Yam, J.C., Chen, L.J., Tham, C.C., Pang, C.P., and Chu, W.K. (2022). Post-Translational Modifications on the Retinoblastoma Protein. *J. Biomed. Sci.* **29**, 33. <https://doi.org/10.1186/s12929-022-00818-x>.
29. Basso, M., Mahuzier, A., Lennon-Duménil, A.-M., Faucourt, M., Meunier, A., Spassky, N., and Delgehyr, N. (2023). Actin-Based Deformations of the Nucleus Control Multiciliated Ependymal Cell Differentiation. Preprint at bioRxiv. <https://doi.org/10.1101/2023.10.13.562225>.
30. Ortiz-Álvarez, G., Fortoul, A., Srivastava, A., Moreau, M.X., Bouloudi, B., Mailhes-Hamon, C., Delgehyr, N., Faucourt, M., Bahin, M., Blugeon, C., et al. (2022). P53/P21 Pathway Activation Contributes to the Ependymal Fate Decision Downstream of GemC1. *Cell Rep.* **41**, 111810. <https://doi.org/10.1016/j.celrep.2022.111810>.
31. Berlucchi, M., De Santi, M.M., Bertoni, E., Spinelli, E., Timpano, S., and Padoan, R. (2012). Ciliary Aplasia Associated with Hydrocephalus: An Extremely Rare Occurrence. *Eur. Arch. Oto-Rhino-Laryngol.* **269**, 2295–2299. <https://doi.org/10.1007/s00405-012-2107-3>.
32. Busquets, R.M., Caballero-Rabasco, M.A., Velasco, M., Lloreta, J., and García-Algar, Ó. (2013). Primary Ciliary Dyskinesia: Clinical Criteria Indicating Ultrastructural Studies. *Arch. Bronconeumol.* **49**, 99.
33. Barlocco, E.G., Valletta, E.A., Canciani, M., Lungarella, G., Gardi, C., De Santi, M.M., and Mastella, G. (1991). Ultrastructural Ciliary Defects in Children with Recurrent Infections of the Lower Respiratory Tract. *Pediatr. Pulmonol.* **10**, 11–17. <https://doi.org/10.1002/ppul.1950100104>.
34. Carlén, B., and Stenram, U. (2005). Primary Ciliary Dyskinesia: A Review. *Ultrastruct. Pathol.* **29**, 217–220. <https://doi.org/10.1080/01913120590951220>.
35. Cerezo, L., and Price, G. (1985). Absence of Cilia and Basal Bodies with Predominance of Brush Cells in the Respiratory Mucosa from a Patient with Immotile Cilia Syndrome (UP 6:45–59, 1984). *Ultrastruct. Pathol.* **8**, 381–382. <https://doi.org/10.3109/01913128509141528>.
36. De Santi, M.M., Gardi, C., Barlocco, G., Canciani, M., Mastella, G., and Lungarella, G. (1988). Cilia-lacking Respiratory Cells in Ciliary Aplasia. *Biol. Cell* **64**, 67–70. [https://doi.org/10.1016/0248-4900\(88\)90094-9](https://doi.org/10.1016/0248-4900(88)90094-9).
37. De Santi, M.M., Magni, A., Valletta, E.A., Gardi, C., and Lungarella, G. (1990). Hydrocephalus, Bronchiectasis, and Ciliary Aplasia. *Arch. Dis. Child.* **65**, 543–544. <https://doi.org/10.1136/adc.65.5.543>.
38. De Boeck, K., Jorissen, M., Wouters, K., Van Der Schueren, B., Eyssen, M., Casteels-VanDaele, M., and Corbeel, L. (1992). Aplasia of Respiratory Tract Cilia. *Pediatr. Pulmonol.* **13**, 259–265. <https://doi.org/10.1002/ppul.1950130416>.
39. Gordon, R.E., and Kattan, M. (1984). Absence of Cilia and Basal Bodies with Predominance of Brush Cells in the Respiratory Mucosa from a Patient with Immotile Cilia Syndrome. *Ultrastruct. Pathol.* **6**, 45–49. <https://doi.org/10.3109/01913128409016664>.
40. Maiti, A.K., Bartoloni, L., Mitchison, H.M., Meeks, M., Chung, E., Spiden, S., Gehrig, C., Rossier, C., DeLozier-Blanchet, C.D., Blouin, J., et al. (2000). No deleterious mutations in the FOXJ1 (alias HFH-4) gene in patients with Primary Ciliary Dyskinesia (PCD). *Cytogenet. Cell Genet.* **90**, 119–122. <https://doi.org/10.1159/000015645>.
41. Matwijiw, I., Thliveris, J.A., and Fairman, C. (1987). Aplasia of Nasal Cilia with Situs Inversus, Azoospermia and Normal Sperm Flagella: A Unique Variant of the Immotile Cilia Syndrome. *J. Urol.* **137**, 522–524. [https://doi.org/10.1016/S0022-5347\(17\)44097-3](https://doi.org/10.1016/S0022-5347(17)44097-3).

42. Gil, Y.R., González, M.A.M., and Orradre, J.L. (2006). Letter to the Editor Ciliary Hypoplasia: A Rare Cause of Ciliary Dyskinesia. *Ultrastruct. Pathol.* 30, 401–402. <https://doi.org/10.1080/01913120600939532>.
43. Wessels, M.W., Avital, A., Failly, M., Munoz, A., Omran, H., Blouin, J.L., and Willems, P.J. (2008). Candidate Gene Analysis in Three Families with Acilia Syndrome. *Am. J. Med. Genet.* 146A, 1765–1767. <https://doi.org/10.1002/ajmg.a.32340>.
44. Gotz, M., and Stockinger, L. (1983). Aplasia of Respiratory Tract Cilia. *Lancet* 321, 1283. [https://doi.org/10.1016/S0140-6736\(83\)92740-X](https://doi.org/10.1016/S0140-6736(83)92740-X).
45. Hawkins, F.J., Suzuki, S., Beermann, M.L., Barillà, C., Wang, R., Villacorta-Martin, C., Berical, A., Jean, J.C., Le Sueur, J., Matte, T., et al. (2021). Derivation of Airway Basal Stem Cells from Human Pluripotent Stem Cells. *Cell Stem Cell* 28, 79–95.e8. <https://doi.org/10.1016/j.stem.2020.09.017>.
46. Soh, B.S., Zheng, D., Li Yeo, J.S., Yang, H.H., Ng, S.Y., Wong, L.H., Zhang, W., Li, P., Nichane, M., Asmat, A., et al. (2012). CD166(Pos) Subpopulation from Differentiated Human ES and iPS Cells Support Repair of Acute Lung Injury. *Mol. Ther.* 20, 2335–2346. <https://doi.org/10.1038/mt.2012.182>.
47. Hall, E.A., Kumar, D., Prosser, S.L., Yeyati, P.L., Herranz-Pérez, V., García-Verdugo, J.M., Rose, L., McKie, L., Dodd, D.O., Tennant, P.A., et al. (2023). Centriolar Satellites Expedite Mother Centriole Remodeling to Promote Ciliogenesis. *eLife* 12, e79299. <https://doi.org/10.7554/eLife.79299>.
48. Sorokin, S.P. (1968). Reconstructions of Centriole Formation and Ciliogenesis in Mammalian Lungs. *J. Cell Sci.* 3, 207–230. <https://doi.org/10.1242/jcs.3.2.207>.
49. Zhao, H., Chen, Q., Li, F., Cui, L., Xie, L., Huang, Q., Liang, X., Zhou, J., Yan, X., and Zhu, X. (2021). Fibrogranular Materials Function as Organizers to Ensure the Fidelity of Multiciliary Assembly. *Nat. Commun.* 12, 1273. <https://doi.org/10.1038/s41467-021-21506-8>.
50. Ma, J.-Y., Ou-Yang, Y.-C., Luo, Y.-B., Wang, Z.-B., Hou, Y., Han, Z.-M., Liu, Z., Schatten, H., and Sun, Q.-Y. (2013). Cyclin O Regulates Germinal Vesicle Breakdown in Mouse Oocytes1. *Biol. Reprod.* 88, 110. <https://doi.org/10.1095/biolreprod.112.103374>.
51. Nigg, E.A., and Holland, A.J. (2018). Once and Only Once: Mechanisms of Centriole Duplication and Their Dereulation in Disease. *Nat. Rev. Mol. Cell Biol.* 19, 297–312. <https://doi.org/10.1038/nrm.2017.127>.
52. Tan, F.E., Vladar, E.K., Ma, L., Fuentealba, L.C., Hoh, R., Espinoza, F.H., Axelrod, J.D., Alvarez-Buylla, A., Stearns, T., Kintner, C., and Krasnow, M.A. (2013). Myb Promotes Centriole Amplification and Later Steps of the Multiciliogenesis Program. *Development* 140, 4277–4286. <https://doi.org/10.1242/dev.094102>.
53. Wang, L., Fu, C., Fan, H., Du, T., Dong, M., Chen, Y., Jin, Y., Zhou, Y., Deng, M., Gu, A., et al. (2013). miR-34b Regulates Multiciliogenesis during Organ Formation in Zebrafish. *Development* 140, 2755–2764. <https://doi.org/10.1242/dev.092825>.
54. Murray, A.W. (2004). Recycling the Cell Cycle: Cyclins Revisited. *Cell* 116, 221–234. [https://doi.org/10.1016/s0092-8674\(03\)01080-8](https://doi.org/10.1016/s0092-8674(03)01080-8).
55. Roig, M.B., Roset, R., Ortet, L., Balsiger, N.A., Anfosso, A., Cabellos, L., Garrido, M., Alameda, F., Brady, H.J.M., and Gil-Gómez, G. (2009). Identification of a Novel Cyclin Required for the Intrinsic Apoptosis Pathway in Lymphoid Cells. *Cell Death Differ.* 16, 230–243. <https://doi.org/10.1038/cdd.2008.145>.
56. Ruiz García, S., Deprez, M., Lebrigand, K., Cavard, A., Paquet, A., Arguel, M.-J., Magnone, V., Truchi, M., Caballero, I., Leroy, S., et al. (2019). Novel Dynamics of Human Mucociliary Differentiation Revealed by Single-Cell RNA Sequencing of Nasal Epithelial Cultures. *Development* 146, dev177428. <https://doi.org/10.1242/dev.177428>.
57. Revinski, D.R., Zaragozi, L.-E., Boutin, C., Ruiz-García, S., Deprez, M., Thomé, V., Rosnet, O., Gay, A.-S., Mercey, O., Paquet, A., et al. (2018). CDC20B Is Required for Deuterosome-Mediated Centriole Production in Multiciliated Cells. *Nat. Commun.* 9, 4668. <https://doi.org/10.1038/s41467-018-06768-z>.
58. Boon, M., Wallmeier, J., Ma, L., Loges, N.T., Jaspers, M., Olbrich, H., Dougherty, G.W., Raidt, J., Werner, C., Amirav, I., et al. (2014). MCIDAS Mutations Result in a Mucociliary Clearance Disorder with Reduced Generation of Multiple Motile Cilia. *Nat. Commun.* 5, 4418. <https://doi.org/10.1038/ncomms5418>.
59. Lu, H., Anujan, P., Zhou, F., Zhang, Y., Chong, Y.L., Bingle, C.D., and Roy, S. (2019). *Mcidas* Mutant Mice Reveal a Two-Step Process for the Specification and Differentiation of Multiciliated Cells in Mammals. *Development* 146, dev172643. <https://doi.org/10.1242/dev.172643>.
60. Stubbs, J.L., Vladar, E.K., Axelrod, J.D., and Kintner, C. (2012). Multicilin Promotes Centriole Assembly and Ciliogenesis during Multiciliate Cell Differentiation. *Nat. Cell Biol.* 14, 140–147. <https://doi.org/10.1038/ncb2406>.
61. Bertoli, C., Skotheim, J.M., and De Bruin, R.A.M. (2013). Control of Cell Cycle Transcription during G1 and S Phases. *Nat. Rev. Mol. Cell Biol.* 14, 518–528. <https://doi.org/10.1038/nrm3629>.
62. Roset, R., and Gil-Gómez, G. (2009). Measurement of Changes in Cdk2 and Cyclin O-Associated Kinase Activity in Apoptosis. In *Apoptosis*, 559, P. Erhardt and A. Toth, eds. (Totowa, NJ: Methods in Molecular Biology; Humana Press), pp. 161–172. https://doi.org/10.1007/978-1-60327-017-5_12.
63. Mercey, O., Al Jord, A., Rostaing, P., Mahuzier, A., Fortoul, A., Boudjema, A.-R., Faucourt, M., Spassky, N., and Meunier, A. (2019). Dynamics of Centriole Amplification in Centrosome-Depleted Brain Multiciliated Progenitors. *Sci. Rep.* 9, 13060. <https://doi.org/10.1038/s41598-019-49416-2>.
64. Moyer, T.C., Clutario, K.M., Lambrus, B.G., Daggubati, V., and Holland, A.J. (2015). Binding of STIL to Plk4 Activates Kinase Activity to Promote Centriole Assembly. *J. Cell Biol.* 209, 863–878. <https://doi.org/10.1083/jcb.201502088>.
65. Hadjantonakis, A.-K., and Papaioannou, V.E. (2004). Dynamic in Vivo Imaging and Cell Tracking Using a Histone Fluorescent Protein Fusion in Mice. *BMC Biotechnol.* 4, 33. <https://doi.org/10.1186/1472-6750-4-33>.
66. Kyrousi, C., Arbi, M., Pilz, G.-A., Pefani, D.-E., Lalioti, M.-E., Ninkovic, J., Götz, M., Lygerou, Z., and Taraviras, S. (2015). *Mcidas* and *GemC1* Are Key Regulators for the Generation of Multiciliated Ependymal Cells in the Adult Neurogenic Niche. *Development* 142, 3661–3674. <https://doi.org/10.1242/dev.126342>.
67. Schindelin, J., Rueden, C.T., Hiner, M.C., and Eliceiri, K.W. (2015). The ImageJ Ecosystem: An Open Platform for Biomedical Image Analysis. *Mol. Reprod. Dev.* 82, 518–529. <https://doi.org/10.1002/mrd.22489>.
68. Gentleman, R.C., Carey, V.J., Bates, D.M., Bolstad, B., Dettling, M., Duoduit, S., Ellis, B., Gautier, L., Ge, Y., Gentry, J., et al. (2004). Open Software Development for Computational Biology and Bioinformatics. *Genome Biol.* 5, R80. <https://doi.org/10.1186/gb-2004-5-10-r80>.
69. Zheng, G.X.Y., Terry, J.M., Belgrader, P., Ryvkin, P., Bent, Z.W., Wilson, R., Ziraldo, S.B., Wheeler, T.D., McDermott, G.P., Zhu, J., et al. (2017). Massively Parallel Digital Transcriptional Profiling of Single Cells. *Nat. Commun.* 8, 14049. <https://doi.org/10.1038/ncomms14049>.
70. Lun, A.T.L., Riesenfeld, S., Andrews, T., Dao, T.P., Gomes, T., and participants in the 1st Human Cell Atlas Jamboree; and Marioni, J.C. (2019). EmptyDrops: Distinguishing Cells from Empty Droplets in Droplet-Based Single-Cell RNA Sequencing Data. *Genome Biol.* 20, 63. <https://doi.org/10.1186/s13059-019-1662-y>.
71. Haghverdi, L., Lun, A.T.L., Morgan, M.D., and Marioni, J.C. (2018). Batch Effects in Single-Cell RNA-Sequencing Data Are Corrected by Matching Mutual Nearest Neighbors. *Nat. Biotechnol.* 36, 421–427. <https://doi.org/10.1038/nbt.4091>.
72. Lun, A.T.L., McCarthy, D.J., and Marioni, J.C. (2016). A Step-by-Step Workflow for Low-Level Analysis of Single-Cell RNA-Seq Data with Bioconductor. *F1000Res.* 5, 2122. <https://doi.org/10.12688/f1000research.9501.2>.
73. McCarthy, D.J., Campbell, K.R., Lun, A.T.L., and Wills, Q.F. (2017). Pre-Processing, Quality Control, Normalization and Visualization of Single-Cell

- RNA-Seq Data in R. *Bioinformatics* 33, 1179–1186. <https://doi.org/10.1093/bioinformatics/btw777>.
74. Aran, D., Looney, A.P., Liu, L., Wu, E., Fong, V., Hsu, A., Chak, S., Naikawadi, R.P., Wolters, P.J., Abate, A.R., et al. (2019). Reference-Based Analysis of Lung Single-Cell Sequencing Reveals a Transitional Profibrotic Macrophage. *Nat. Immunol.* 20, 163–172. <https://doi.org/10.1038/s41590-018-0276-y>.
 75. Street, K., Risso, D., Fletcher, R.B., Das, D., Ngai, J., Yosef, N., Purdom, E., and Dudoit, S. (2018). Slingshot: Cell Lineage and Pseudotime Inference for Single-Cell Transcriptomics. *BMC Genom.* 19, 477. <https://doi.org/10.1186/s12864-018-4772-0>.
 76. Kolberg, L., Raudvere, U., Kuzmin, I., Vilo, J., and Peterson, H. (2020). Gprofiler2 – an R Package for Gene List Functional Enrichment Analysis and Namespace Conversion Toolset g:Profiler. *F1000Res.* 9, ELIXIR-709. <https://doi.org/10.12688/f1000research.24956.2>.
 77. Hao, Y., Stuart, T., Kowalski, M.H., Choudhary, S., Hoffman, P., Hartman, A., Srivastava, A., Molla, G., Madad, S., Fernandez-Granda, C., and Satija, R. (2024). Dictionary Learning for Integrative, Multimodal and Scalable Single-Cell Analysis. *Nat. Biotechnol.* 42, 293–304. <https://doi.org/10.1038/s41587-023-01767-y>.
 78. Van den Berge, K., Roux de Bézieux, H., Street, K., Saelens, W., Cannoodt, R., Saeys, Y., Dudoit, S., and Clement, L. (2020). Trajectory-Based Differential Expression Analysis for Single-Cell Sequencing Data. *Nat. Commun.* 11, 1201. <https://doi.org/10.1038/s41467-020-14766-3>.
 79. Bergen, V., Lange, M., Peidli, S., Wolf, F.A., and Theis, F.J. (2020). Generalizing RNA Velocity to Transient Cell States through Dynamical Modeling. *Nat. Biotechnol.* 38, 1408–1414. <https://doi.org/10.1038/s41587-020-0591-3>.
 80. Wickham, H. Ggplot2. 2009. 10.1007/978-0-387-98141-3.[CrossRef] [CS: 100]
 81. Wickham, H., Averick, M., Bryan, J., Chang, W., McGowan, L., François, R., Grolemund, G., Hayes, A., Henry, L., Hester, J., et al. (2019). Welcome to the Tidyverse. *J. Open Source Softw.* 4, 1686. <https://doi.org/10.21105/joss.01686>.
 82. Conant, D., Hsiau, T., Rossi, N., Oki, J., Maures, T., Waite, K., Yang, J., Joshi, S., Kelso, R., Holden, K., et al. (2022). Inference of CRISPR Edits from Sanger Trace Data. *CRISPR J.* 5, 123–130. <https://doi.org/10.1089/crispr.2021.0113>.
 83. Delgehyr, N., Meunier, A., Faucourt, M., Bosch Grau, M., Strehl, L., Janke, C., and Spassky, N. (2015). Ependymal Cell Differentiation, from Monociliated to Multiciliated Cells. *Methods Cell Biol.* 127, 19–35. <https://doi.org/10.1016/bs.mcb.2015.01.004>.
 84. Jeffrey, P.D., Russo, A.A., Polyak, K., Gibbs, E., Hurwitz, J., Massagué, J., and Pavletich, N.P. (1995). Mechanism of CDK Activation Revealed by the Structure of a cyclinA-CDK2 Complex. *Nature* 376, 313–320. <https://doi.org/10.1038/376313a0>.
 85. Kiselev, V.Y., Yiu, A., and Hemberg, M. (2018). Projection of Single-Cell RNA-Seq Data across Data Sets. *Nat. Methods* 15, 359–362. <https://doi.org/10.1038/nmeth.4644>.
 86. Hao, Y., Hao, S., Andersen-Nissen, E., Mauck, W.M., Zheng, S., Butler, A., Lee, M.J., Wilk, A.J., Darby, C., Zager, M., et al. (2021). Integrated Analysis of Multimodal Single-Cell Data. *Cell* 184, 3573–3587.e29. <https://doi.org/10.1016/j.cell.2021.04.048>.
 87. Xu, J., Falconer, C., Nguyen, Q., Crawford, J., McKinnon, B.D., Mortlock, S., Senabouth, A., Andersen, S., Chiu, H.S., Jiang, L., et al. (2019). Genotype-Free Demultiplexing of Pooled Single-Cell RNA-Seq. *Genome Biol.* 20, 290. <https://doi.org/10.1186/s13059-019-1852-7>.
 88. Love, M.I., Huber, W., and Anders, S. (2014). Moderated Estimation of Fold Change and Dispersion for RNA-Seq Data with DESeq2. *Genome Biol.* 15, 550. <https://doi.org/10.1186/s13059-014-0550-8>.
 89. Wu, T., Hu, E., Xu, S., Chen, M., Guo, P., Dai, Z., Feng, T., Zhou, L., Tang, W., Zhan, L., et al. (2021). clusterProfiler 4.0: A Universal Enrichment Tool for Interpreting Omics Data. *Innovation* 2, 100141. <https://doi.org/10.1016/j.xinn.2021.100141>.
 90. Vallier, L., Touboul, T., Chng, Z., Brimpari, M., Hannan, N., Millan, E., Smithers, L.E., Trotter, M., Rugg-Gunn, P., Weber, A., and Pedersen, R.A. (2009). Early Cell Fate Decisions of Human Embryonic Stem Cells and Mouse Epiblast Stem Cells Are Controlled by the Same Signalling Pathways. *PLoS One* 4, e6082. <https://doi.org/10.1371/journal.pone.0006082>.
 91. McCauley, K.B., Hawkins, F., Serra, M., Thomas, D.C., Jacob, A., and Kotton, D.N. (2017). Efficient Derivation of Functional Human Airway Epithelium from Pluripotent Stem Cells via Temporal Regulation of Wnt Signaling. *Cell Stem Cell* 20, 844–857.e6. <https://doi.org/10.1016/j.stem.2017.03.001>.

STAR★METHODS

KEY RESOURCES TABLE

REAGENT or RESOURCE	SOURCE	IDENTIFIER
Antibodies		
Mouse IgG1 Monoclonal Anti-Polyglutamylated Modification (GT335)	AdipoGen	Cat# AG-20B-0020; Clone GT335; RRID: AB_2490210
Mouse IgG1 Monoclonal Anti-Active-beta-Catenin (anti-ABC)	Millipore	Cat# 05-665; Clone 8E7; RRID: AB_309887
Rabbit Anti-CCNO, raised against the peptide H-SSLPRILPPQIWERC-NH ₂ present at the C terminus of mouse cyclin O sequence	Gift from the laboratory of Gabriel Gil-Gómez ⁶²	N/A
Mouse IgG2b Monoclonal Anti FOP (FGFR1OP)	Abnova Corporation	Cat# H00011116-M01; Clone: 2B1; RRID: AB_463883
Mouse IgG1 Monoclonal Anti FoxJ1	Thermo Fisher Scientific	Cat# 14-9965-82; Clone: 2A5; RRID: AB_1548835
Rabbit Polyclonal Anti-p27	Santa Cruz Biotechnology	Cat# sc-528; RRID: AB_632129
Rabbit Monoclonal Anti Phospho-Rb (Ser807/811)	Cell Signaling Technology	Cat# 8516; Clone D20B12; RRID: AB_11178658
Rabbit Polyclonal Anti Deup1	Homemade in the laboratory of Nathalie Spassky; raised against the peptide TKLKQSRHI ⁶³	N/A
Mouse IgG2b Monoclonal Anti SAS-6 (91.390.21)	Santa Cruz Biotechnology	Cat# sc-81431; RRID: AB_1128357
Rabbit Polyclonal Anti-PLK4 conjugated to fluorophore DyLight 550	Gift from the laboratory of Andrew J. Holland ⁶⁴	N/A
Chicken Polyclonal Anti GFP	Aves Labs	Cat# GFP-1020; RRID: AB_10000240
Mouse IgG1 Monoclonal Anti-Human ALCAM Phycoerythrin (Clone 105902)	R&D Systems	Cat# FAB6561P; RRID: AB_2223887
Mouse IgG1 Monoclonal APC anti-human CD271 (NGFR)	BioLegend	Cat# 345108; RRID: AB_10645515
Mouse IgG2b Monoclonal PE anti-human CD326 (Ep-CAM)	BioLegend	Cat# 324206; RRID: AB_756080
Rabbit Polyclonal Anti-CCNO	Atlas Antibodies	Cat# HPA050090; RRID: AB_2681011
Goat Polyclonal Anti-Human Nanog	R&D Systems	Cat# AF1997; RRID: AB_355097
Mouse Monoclonal Anti- Fetoprotein, alpha (AFP) Unconjugated, Clone C3	Sigma-Aldrich	Cat# A8452; RRID: AB_258392
Mouse IgG2a Monoclonal Anti-Smooth Muscle Actin (a-SM1)	Thermo Fisher Scientific	Cat# MA1-12772, RRID: AB_1087373
Mouse Monoclonal Anti-Neuronal Class III beta-Tubulin (TUJ1)	Covance	Cat# MMS-435P; RRID: AB_2313773
Rabbit Monoclonal Anti-HA-Tag (C29F4)	Cell Signaling Technology	Cat# 3724; RRID: AB_1549585
Mouse IgG2a Monoclonal Anti-Beta Tubulin	Proteintech	Cat# 66240-1-Ig; RRID: AB_2881629
Rabbit Anti-RFX2	Sigma-Aldrich	Cat# HPA048969; RRID: AB_2680577
Rabbit Polyclonal Anti-RFX3	Atlas Antibodies	Cat# HPA035689; RRID: AB_10671224
Anti-myc tag 9E10	Roig et al. ⁵⁵	N/A
Goat anti-Mouse IgG1 Cross-Adsorbed Secondary Antibody, Alexa Fluor 488	Thermo Fischer Scientific	Cat# A-21121; RRID: AB_2535764
Goat anti-Mouse IgG1 Cross-Adsorbed Secondary Antibody, Alexa Fluor 594	Thermo Fisher Scientific	Cat# A-21125; RRID: AB_2535767

(Continued on next page)

Continued

REAGENT or RESOURCE	SOURCE	IDENTIFIER
Goat anti-Mouse IgG1 Cross-Adsorbed Secondary Antibody, Alexa Fluor 647	Thermo Fisher Scientific	Cat# A-21240; RRID: AB_2535809
Donkey anti-Rabbit IgG (H + L) Highly Cross-Adsorbed Secondary Antibody, Alexa Fluor 488	Thermo Fisher Scientific	Cat# A-21206, RRID: AB_2535792
Donkey anti-Rabbit IgG (H + L) Highly Cross-Adsorbed Secondary Antibody, Alexa Fluor 594	Thermo Fisher Scientific	Cat# A-21207; RRID: AB_141637
Donkey anti-Rabbit IgG (H + L) Highly Cross-Adsorbed Secondary Antibody, Alexa Fluor 647	Thermo Fisher Scientific	Cat# A-31573; RRID: AB_2536183
Goat anti-Mouse IgG2b Cross-Adsorbed Secondary Antibody, Alexa Fluor 488	Thermo Fisher Scientific	Cat# A-21141; RRID: AB_2535778
Goat anti-Mouse IgG2b Cross-Adsorbed Secondary Antibody, Alexa Fluor 568	Thermo Fisher Scientific	Cat# A-21144; RRID: AB_2535780
Goat anti-Mouse IgG2b Cross-Adsorbed Secondary Antibody, Alexa Fluor 647	Thermo Fisher Scientific	Cat# A-21242; RRID: AB_2535811
Donkey anti-Chicken IgY (IgG) (H + L) AffiniPure, Alexa Fluor 488	Jackson ImmunoResearch Labs	Cat# 703-545-155; RRID: AB_2340375
Donkey anti-Rabbit IgG (H + L) Highly Cross-Adsorbed Secondary Antibody, Alexa Fluor 546	Thermo Fisher Scientific	Cat# A10040; RRID: AB_2534016
Donkey anti-Mouse IgG (H + L) Highly Cross-Adsorbed Secondary Antibody, Alexa Fluor Plus 488	Thermo Fisher Scientific	Cat# A32766; RRID: AB_2762823
Goat anti-Mouse IgG (H + L) Cross-Adsorbed Secondary Antibody, Alexa Fluor 488	Thermo Fisher Scientific	Cat# A-11001; RRID: AB_2534069
Bacterial and virus strains		
XL-10 gold ultracompetent <i>E. coli</i> cells	Agilent Technologies	200315
Biological samples		
Adult lung mRNA (Total RNA – Human Adult Normal Tissue: Lung lower left lobe)	Biochain	Cat #R1234152-50; Lot #B6050780
Fetal Bovine Serum	Hyclone	SH30071.01
Chemicals, peptides, and recombinant proteins		
Hoechst (bisBenzimide H 33342 trihydrochloride)	Merck	Cat# B2261; CAS: 875756-97-1
DAPI	Invitrogen	D1306
Blasticidin	Sigma-Aldrich	203350
Activin A	R&D Systems	338-AC
FGF2	R&D Systems	233-FB
LY294002	Promega	V1201
CHIR99021	Tocris Bioscience	4423
BMP4	R&D Systems	314-BP
SB431542	Tocris Bioscience	1614
Dorsomorphin	Tocris Bioscience	3093
B27	Gibco	17504044
Non-essential amino acids (NEAA)	Gibco	11140050
FGF7	Peprotech	100-19-10UG
FGF10	Peprotech	100-26-5UG
Retinoic acid	Sigma-Aldrich	R2625
Dexamethasone	Sigma-Aldrich	D4902

(Continued on next page)

Continued

REAGENT or RESOURCE	SOURCE	IDENTIFIER
8-Bromoadenosine 30,50-cyclic monophosphate sodium salt (cAMP)	Sigma-Aldrich	B7880
3-Isobutyl-1-methylxanthine (IBMX)	Sigma-Aldrich	I7018
A 83-01	Stemcell Technologies	100-0245
Polyvinyl alcohol	Sigma	P8136-250G
Conc. Lipids	Life Technologies	1190531
Transferrin	Sigma	T1147
Insulin	Roche	1376497
HEPES	Thermofisher	15630080
GlutaMAX	Life Technologies	35050-061
N-2	Life Technologies	17502-048
β-Mercaptoethanol	Sigma	M6250
L-Glutamine	Life Technologies	25030024
Lipofectamine Stem Reagent	Life Technologies	STEM0015
Ampicillin Sodium Salt	Sigma	A9518
Critical commercial assays		
jetPRIME®	Polyplus	101000027
QIAamp DNA Mini Kit	Qiagen	51304
RNeasy Mini Kit	Qiagen	74106
High-Capacity cDNA Reverse Transcription Kit	Applied Biosystems	4368814
Nucleofection Amaxa P3 primary cell 4D Nucelofector Kit	Lonza	V4XP-3024
QIAprep spin miniprep	Qiagen	27106
Zymopure II Plasmid Maxiprep	Zymopure	D4203-B
Deposited data		
Raw and analyzed scRNA-seq data	This paper	GEO: GSE201773; cellxgene collection # 33f48a52-31d8-4cc8-bd00-1e89c659a87f
Original code for this study	This paper	https://doi.org/10.5281/zendodo.14105247
Experimental models: Cell lines		
H9	WiCell	WAe009-A
HEK293T	ATCC	CRL-3216
Experimental models: Organisms/strains		
RjORL:SWISS	Janvier Labs	N/A
<i>Ccno</i> ^{RA}	Gift from the laboratory of Sebastian J. Arnold ¹⁹	N/A
<i>Ccno</i> ^{KO}	Gift from the laboratory of Gabriel Gil-Gómez ²⁰	N/A
Oligonucleotides		
CRISPR sgRNA3 hCCNO ACTCGAAGGAGAG GCCGAATTGG	This paper	N/A
Genotyping primer hCCNO F1 atggtgacccccc tgtccca	This paper	N/A
Genotyping primer hCCNO R1 ttatttcgagctcg ggggcaag	This paper	N/A
Insertion of FLAG tag at N terminus EcoRI-Flag-hCCNO F1 GACGACGATGACAAGgtga ccccctgtccccac	This paper	N/A

(Continued on next page)

Continued

REAGENT or RESOURCE	SOURCE	IDENTIFIER
Insertion of FLAG tag at N terminus EcoRI-Flag-hCCNO F2 CATGGACTACAAGGACGA CGATGACAAGtgacc	This paper	N/A
Insertion of FLAG tag at N terminus EcoRI-Flag-hCCNO F3 tcagGAATTGCCACCATGGA CTACAAGGACGACGAT	This paper	N/A
Insertion of FLAG tag at N terminus hCCNO-XbaI R1 tcagTCTAGAtttcgagctggggcag	This paper	N/A
Insertion of HA tag at C terminus SacI-Ha-XbaI Oligo 1 cgaaaTACCCATACGATGTTCC AGATTACGCTaaT	This paper	N/A
Insertion of HA tag at C terminus SacI-Ha-XbaI Oligo 2 CTAGAttaAGCGTAATCTGGAACAT CGTATGGGTAtttcgact	This paper	N/A
Primers for RT-qPCR of CCNO forward sequence TCTACAGACCTCCCGCGACT reverse sequence AAGGGACTTCCTGTAACAATGCA	This paper	N/A
Recombinant DNA		
pCAG-H2B-GFP Plasmid	Gift from the laboratory of Xavier Morin ⁶⁵	N/A
pCAGGS-Mcidas Plasmid	Gift from the laboratory of Stavros Taraviras ⁶⁶	N/A
pHF1-Cas9-sgRNA	Gift from the laboratory of Norris Ray Dunn	N/A
pCS2+ Plasmid	RZPD	N/A
pCAGGS-GemC1 Plasmid	Gift from the laboratory of Stavros Taraviras ⁶⁶	N/A
pcDNA3myc-hCyclinO Plasmid	Gift from the laboratory of Gabriel Gil-Gómez	N/A
pWPI-LinkerB Plasmid	Gift from the laboratory of Gabriel Gil-Gómez	N/A
pWPI-mCCNO WT Plasmid	Gift from the laboratory of Gabriel Gil-Gómez	N/A
pWPI-mCCNO K190A Plasmid	Gift from the laboratory of Gabriel Gil-Gómez	N/A
pWPI-mCCNO R135A Plasmid	Gift from the laboratory of Gabriel Gil-Gómez	N/A
Software and algorithms		
ImageJ	Schindelin et al. ⁶⁷	https://ImageJ.nih.gov/ij/download.html ; RRID: SCR_003070
GraphPad Prism 10	GraphPad Prism for Windows, GraphPad Software, La Jolla California USA	https://www.graphpad.com/ ; RRID: SCR_002798
R v4.4.1	R-project	https://www.r-project.org/
Bioconductor v3.19	Gentleman et al. ⁶⁸	https://www.bioconductor.org/
10x Genomics Cell Ranger v5.0.1	Zheng et al. ⁶⁹	https://www.10xgenomics.com/support/software/cell-ranger/latest
DropletUtils 1.24.0	Lun et al. ⁷⁰	https://www.bioconductor.org/
batchelor 1.20.0	Haghverdi et al. ⁷¹	https://www.bioconductor.org/
scran 1.32.0	Lun et al. ⁷²	https://www.bioconductor.org/
scater 1.32.0	McCarthy et al. ⁷³	https://www.bioconductor.org/
scuttle 1.14.0	McCarthy et al. ⁷³	https://www.bioconductor.org/

(Continued on next page)

Continued

REAGENT or RESOURCE	SOURCE	IDENTIFIER
igraph 2.0.3	Csardi et al. 2006	https://cran.r-project.org/web/packages/igraph/index.html
SingleR 2.6.0	Aran et al. ⁷⁴	https://www.bioconductor.org/
slingshot 2.12.0	Street et al. ⁷⁵	https://www.bioconductor.org/
gprofiler2 0.2.3	Kolberg et al. ⁷⁶	https://cran.r-project.org/web/packages/gprofiler2/index.html
Seurat 5.1.0	Hao et al. ⁷⁷	https://cran.r-project.org/web/packages/Seurat/index.html
tradeSeq 1.18.0	Van den Berg et al. ⁷⁸	https://www.bioconductor.org/
scvelo 0.2.5	Bergen et al. ⁷⁹	https://scvelo.readthedocs.io/en/stable/
ggplot2 3.5.1	Whickam ⁸⁰	https://cran.r-project.org/web/packages/ggplot2/index.html
tidyverse 2.0.0	Whickam et al. ⁸¹	https://cran.r-project.org/web/packages/tidyverse/index.html
Inference of CRISPR Edits	Conant et al. ⁸²	N/A

EXPERIMENTAL MODEL AND STUDY PARTICIPANT DETAILS

Transgenic mice

All animal studies were performed in accordance with the guidelines of the European Community and French Ministry of Agriculture and were approved by the “Direction départementale de la protection des populations de Paris” (Approval number Ce5/2012/107; APAFiS #9343). Most of the mouse strains have already been described: *Ccno*^{RA} are from Sebastian J. Arnold’s laboratory¹⁹ and *Ccno*^{KO} are from Gabriel Gil-Gómez’s laboratory.²⁰ Wild-type are either RjOrl:SWISS (Janvier labs), or the WT and/or HT pups from the same litters as the different *Ccno* mutants.

Human embryonic stem cell (hESC) culture

All experiments with the human embryonic stem cell line H9 were approved by the institutional biosafety committee (approval number: HSE-IBC+GMAC-SR-10).

Human patients

Patients A to I

In accordance with the Declaration of Helsinki and French législation, the patients or their legal representatives provided a written informed consent. A standardized form was used to collect clinical features to ensure consistency and accuracy in data collection. Patients’ information can be found in Tables S1 and S2.

Patients J to T

We obtained signed and informed consent from the patients according to protocols approved by the ethic committee of the University of Muenster and Freiburg. The patients OP-1246 II1, OP-642 II1, OP-151 II1, OP-971 II1, OP-1367 II1, OP-1777 I5, OP-1777 II1, OP-1777 II2, OI-66 II1 and OI-104 II1 had been reported recently.^{13,58} In patient OP-1977 II1 we identified the gene variant CCNO c.258_262dup p.(Gln88Argfs*8). Patients’ information can be found in Table S2.

METHOD DETAILS

Primary brain ependymal cell cultures and transfections

The ependymal culture has been previously described.⁸³ Briefly, newborn mice (P0-P2) were sacrificed by decapitation. The brains were dissected in Hank’s solution (10% HBSS, 5% HEPES, 5% sodium bicarbonate, 1% Penicillin/Streptomycin (P/S) in pure water) and the telencephalon were cut manually into pieces, followed by enzymatic digestion (DMEM glutamax, 33% papain (Worthington 3126), 17% DNase at 10 mg/mL, 42% cysteine at 12 mg/mL) for 45 min at 37°C in a humidified 5% CO₂ incubator. Digestion was stopped by addition of a solution of trypsin inhibitors (Leibovitz Medium L15, 10% ovomucoid at 1 mg/mL, 2% DNase at 10 mg/mL). The cells were then washed in L15 and resuspended in DMEM glutamax supplemented with 10% fetal bovine serum (FBS) and 1% P/S in a Poly-L-lysine (PLL)-coated flask. Ependymal progenitors proliferated for 4–5 days until confluence before shaking (250rpm) overnight. Pure confluent astroglial monolayers were replated at a density of 7,5×10³ cells/µL (corresponding to days *in vitro* “DIV” –1) in DMEM glutamax, 10% FBS, 1% P/S on PLL coated coverslides for immunofluorescence experiments and

maintained overnight. The medium was then replaced by serum-free DMEM glutamax 1% P/S, to trigger ependymal differentiation *in vitro* (DIV 0). Transfections were performed in suspension at DIV -1 using the Jetprime (Polyplus) system, plasmids are listed in the [key resources table](#).

Validation of CCNO CDK-dead expressing plasmids pWPI-mCCNO R135A and pWPI-mCCNO K190A

Since CCNO was shown to bind and activate CDK1 and CDK2 when expressed in HEK293,⁵⁵ we mutated residues K190 and R135A (corresponding to K266 and R211 of the human Cyclin A2 sequence, respectively), which are highly conserved residues characteristic of the cyclin fold, the protein domain that allows its interaction with the corresponding CDKs.⁸⁴ HEK293 cells were transiently transfected with vectors expressing myc-tagged WT or mutant CCNO. Immunoprecipitation and Histone H1 kinase assays were done as detailed for CCNO WT in Roig et al.⁵⁵ Briefly, 48h after transfection, cell extracts were prepared and the transfected proteins immunoprecipitated using anti-myc tag antibodies (9E10, Roig et al.⁵⁵). The immunoprecipitates were incubated with purified Histone H1 and ³²P-ATP, the proteins resolved by SDS-PAGE and phosphoproteins detected by autoradiography, showing a lack of activity of the immunoprecipitates formed with CCNO mutated on residues R135A or K190A compared to immunoprecipitates formed with WT CCNO ([Figure S9B](#)). To control for expression of the transfected proteins, 1/20th of each lysate was immunoblotted against the 9E10 antibody. A non-specific band recognized by the antibody is shown as a lysate loading control.

Immunostainings

Brain lateral ventricles and tracheal samples were permeabilized in PBS 1X with 0.1% and 0.5% Triton X-100 solutions, respectively, for 1 min at RT, then fixed in methanol at -20°C for 7 min. Cell cultures were fixed in methanol at -20°C for 10 min or PFA 4% at RT for 10 min. Tissues and cells were pre-blocked in PBS 1X with 0.2% Triton X-100 and 10% FBS (blocking solution) before incubation with primary then secondary antibodies. All these were incubated overnight at 4°C or for 1h at RT in the primary antibodies diluted in blocking solution. The primary antibodies (see [key resources table](#)) used are mouse IgG1 anti Polyglutamyl modification (GT335, 1:1000), mouse IgG1 anti active-beta-catenin (1:500), rabbit anti-CCNO (1:20), mouse IgG2b anti FOP (1:1000), mouse IgG1 anti FoxJ1 (1:700), rabbit anti p27kip1 (1:200), rabbit anti phospho Rb (1:1000), rabbit anti Deup1 (1:5000), mouse IgG2b anti SAS6 (1:700), rabbit anti Plk4 (1:1000). Nuclei were counterstained with a 1:1500 Hoechst solution (from a 20 mg/mL stock), containing the secondary antibodies for 1h at RT. The secondary antibodies are species-specific Alexa Fluor secondary antibodies (1:400). Finally, the wholemounts were redissected to keep only the thin lateral walls of the LV⁸³ which were mounted with Fluoromount-G mounting medium (Southern Biotech, 0100-01). Cell cultures on coverslips were mounted on glass slides with Fluoromount-G. Fluoromount-mounted slides were stored at 4°C.

Microscopy

Epifluorescence microscopy

Fixed cells were examined with an upright epifluorescence microscope (Zeiss Axio Observer.Z1) equipped with an Apochromat ×63 (NA 1.4) oil-immersion objective and a Zeiss Apotome with an H/D grid. Images were acquired using Zen with 500-nm z-steps. When better resolution was needed, confocal image stacks were collected with a 63 x/1.4 Oil objective on an inverted LSM 880 Airyscan Zeiss microscope with 440, 515, 560 and 633 laser lines with 180 or 250-nm z-steps and Zen2 software with Airyscan mode z stack projections are shown for all epifluorescence microscopy images.

Transmission electron microscopy

Cultured cells were fixed in 2.5% glutaraldehyde and 4% PFA, treated with 1% OsO₄, washed and progressively dehydrated. The samples were then incubated in 1% uranyl acetate in 70% methanol, before final dehydration, pre-impregnation with ethanol/epoxy (2/1, 1/1, 1/2) and impregnation with epon resin. After mounting in epon blocks for 48 h at 60°C to ensure polymerization, ultra-thin sections (70 nm) were cut on an ultramicrotome (Ultracut E, Leica) and analyzed using a Philips Technai 12 transmission electron microscope.

Single-cell RNA-seq of *in vitro* differentiating multiciliated cells

Single-cell RNA-seq of *in vitro* WT differentiating multiciliated cells was described previously.¹¹ For *Ccno*^{KO}, newborn mice (P0-P2) were sacrificed and cultured in the mean time as their WT littermates (the C57Bl6N WT replicate used in Serizay et al., 2024¹¹). After 2 days of *in vitro* differentiation, flasks were rinsed with PBS 1X twice and treated by enzymatic cell dissociation (Trypsin, 1mL) for 10 min and trituration to obtain a single cell suspension. Digestion was stopped by addition of 1 mL of fetal bovine serum (FBS). The cells were then washed in serum-free DMEM glutamax 1% P/S and resuspended in HBSS-0.1% BSA for single-cell RNA-seq library preparation. Cell cultures from three different animals with the same genetic background and treatment were pooled together; to multiplex them, samples were labeled using a cell surface protein labeling strategy following manufacturer's instructions (https://assets.ctfassets.net/an68im79xiti/5KA1NbZdTOam8A0yq6KyC2/f3e0479ff7b1c1633e6ddf8959a88a3bCG000149_DemonstratedProtocol_CellSurfaceProteinLabeling_Rev_A.pdf), using TotalSeq hashtag antibodies (BioLegend). However, the efficiency of the cell hashing did not allow to unambiguously separate cells coming from different animals and was therefore not directly used in downstream analysis. Cell suspensions were passed through a 40 µm Flowmi cell strainer (BelArt) and cell concentrations were carefully evaluated with a Countess FL automated cell counter (Thermofisher). For single cell RNA-seq, cells were partitioned with a Chromium equipment (10X Genomics) and libraries were prepared using the standard Single Cell 3' v3.1 protocol

(10X Genomics). Sequencing was performed on an Illumina NextSeq 500 sequencing machine following manufacturer's instructions, on a high Flowcell, using the following sequencing cycles: 28b for read 1, 55b for read 2, 8b for index.

Computational analysis of single-cell RNA-seq data

Pre-processing of scRNA-seq of *in vitro* differentiating multiciliated *Ccno*^{KO} cells

Pre-processing of scRNA-seq of *in vitro* differentiating multiciliated *Ccno*^{KO} cells was done as described for WT cells in Serizay et al., 2024.¹¹ Briefly, Fastq file demultiplexing, barcode processing, gene counting, and aggregation were made using the Cell Ranger software following 10X Genomics guidelines. 10X Genomics mm10 genome reference and gene annotations compiled in 2020 were used (https://support.10xgenomics.com/single-cell-gene-expression/software/release-notes/build#mm10_2020A). Empty cells (detected by emptyDrops from DropletUtils) were filtered out and only protein-coding genes were retained.

Annotation transfer and UMAP projection between WT and *Ccno*^{KO} scRNA-seq datasets

scmap package⁸⁵ was used to transfer cluster annotations from WT to *Ccno*^{KO} cells. For visualization, projection of the *Ccno*^{KO} cells onto the WT UMAP embedding¹¹ was performed using Seurat⁸⁶ (Figure S3A).

Merging WT or *Ccno*^{KO} scRNA-seq datasets

Genotype correction and merging of WT¹¹ and *Ccno*^{KO} single-cell RNA-seq datasets was performed using fast MNN correction from batchelor package,⁷¹ using genes found enriched (fold-change >2, adjusted *p*-value ≤ 0.05) in any of the annotated/transferred clusters with scran package.⁷²

Cell cycle phase annotation of merged WT or *Ccno*^{KO} cells

Putative cell cycle phases were transferred from a recent scRNA-seq dataset of proliferating neural stem cells with annotated cell cycle phases²² using SingleR.⁷⁴ G0, G1 and Late G1 labels were collapsed to a single "G0/G1" label.

Trajectory analysis of merged WT or *Ccno*^{KO} cells

Trajectory and pseudotime inferences were performed using the shared MNN-corrected PCA embedding of merged WT and *Ccno*^{KO} cells (Figure S3B) with slingshot,⁷⁵ specifying start (proliferating progenitors) and end clusters (terminally differentiated MCCs) to orientate the trajectory. Computed pseudotime was scaled between 0 and 1 for clarity. Continuous gene expression along the slingshot-inferred trajectory was modeled using a generalized additive model.

Characterization of primordial deuterosomal cells in WT or *Ccno*^{KO} scRNA-seq datasets

The pseudotime value containing 95% of all *Ccno*^{KO} cells was determined, and subsequently used to split the original "Early Deuterosomal Cells" cluster (Figure S3A) into "Primordial deuterosomal" and "Early deuterosomal" cells (Figures 3A and S3C).

Ccno^{KO} vs. WT differential gene expression analysis was performed specifically on cells from the "Primordial deuterosomal" cluster. To control for technical variations between individuals and/or replicates, we first phased each cell in each dataset (3 individuals pooled for each of the 2 WT replicates,¹¹ and 3 individuals pooled in the *Ccno*^{KO} dataset) using scSplit.⁸⁷ I then used the phasing and the replicate annotations to group WT (*Ccno*^{KO}) primordial deuterosomal into 6 (3) meta-cells using the 'aggregateAcrossCells' function from the scuttle package. Each meta-cell thus contains cells from a separate individual, with a specific genetic background. I then performed a differential expression analysis on these pseudo-bulk meta-cells using DESeq2,⁸⁸ treating the replicate and genetic background as confounding variables. Genes differentially expressed between *Ccno*^{KO} and WT primordial deuterosomal cells (absolute fold-change >2, adjusted *p*-value ≤ 0.1) were finally recovered. GSEA was performed with clusterProfiler.⁸⁹

Generation of human epithelial airway cells from human embryonic stem cell (hESC)

Human embryonic stem cell (hESC) culture

H9 hESCs were routinely cultured on vitronectin-coated tissue culture dishes in Essential 8 (E8) medium (Life Technologies) in an incubator with 5% CO₂, at 37°C.

Construction of CRISPR sgRNA vectors and donor template

Three CRISPR sgRNAs, targeting exons 1 and 2, of the human CCNO gene were designed using CHOPCHOP (<https://chopchop.cbu.uib.no/>) and cloned into the pHF1-Cas9 plasmid. The sgRNA sequences are provided in the key resources table.

Nucleofection

H9 cells were dissociated into single cells with Accutase (Stem Cell Technologies). Two million cells were mixed with 10 µg pHF1-Cas9-sgRNA and nucleofected using the Lonza Amaxa 4D Nucleofector (Lonza). E8 medium supplemented with 5.25 µg/mL Blasticidin was applied to the cells 24 h post-nucleofection. Cells were fed E8 media every day until colonies were large enough for picking and genotyping.

Genotyping

To extract genomic DNA, picked colonies were incubated for 55°C for 1 h followed by a 5 min incubation at 95°C in a 20 µL reaction containing 1X detergent (0.05% IGEPAL CA630, 0.05% Tween 20), proteinase K and 1X TE buffer. 1 µL of genomic DNA was used in a PCR reaction containing 1X PrimeStar Max Mastermix (Takara) and genotyping primers. The thermal cycling conditions used were as follows: 10 s at 98°C, followed by 35 cycles of 10 s at 98°C, 5 s at 55°C and 1 min at 72°C. The PCR products were then sent to Bio Basic Asia Pacific Pte Ltd for sequencing. Genotyping primer sequences are listed in the key resources table.

Clonal expansion

H9 clones with frameshift mutations were dissociated into single cells using Accutase and seeded onto vitronectin-coated plates in E8 medium supplemented with CloneR (Stem Cell Technologies). Cells were fed with fresh E8 medium daily until colonies grew large enough for picking and genotyping. Clones with homozygous frameshift mutations were expanded and frozen stocks were made using Cryostor (Stem Cell Technologies).

Construction of wild-type (WT) and mutant CCNO expression vectors

WT and mutant CCNO cDNA (c.431_444del) were cloned into the pCS2+ expression vector. FLAG tags were added to the N termini and HA tags were added to the C termini of both WT and mutant sequences. Primer sequences are provided in the [key resources table](#).

Transfection of HEK293T cells

500,000 HEK293T cells were seeded onto wells of a 6-well plate in MEF media and allowed to attach overnight in an incubator at 37°C. The following day, cells were transfected with 1 µg pCS2+CCNO WT, pCS2+CCNO c.431_444del or pCS2+eGFP using Lipofectamine 2000 (Life technologies). Cells were harvested for Western blotting or immunofluorescence 48 h-post transfection.

Trilineage differentiation

H9 cells were dissociated into small clumps using Accutase (Stem Cell Technologies) and collected in a falcon tube. Cells were collected into a pellet by centrifugation at 1200 rpm for 5 min. The cell pellet was resuspended in MEF medium (15% FBS, 1% Glutamax in DMEM F12 Advanced), and the resulting cell suspension transferred into low adhesion tissue culture dishes to form embryoid bodies. The medium was changed every other day for 7 days. The embryoid bodies formed were collected and plated onto 0.1% gelatin-coated tissue culture dishes. Cellular outgrowths were fed every other day with fresh MEF medium for a further 7 days before they were fixed with 4% paraformaldehyde for analysis by immunofluorescence.

Karyotype analysis

H9 CCNO subclones, 52-3 and 20-1 cultured to 70–80% confluence, were sent to the KK Women's and Children's Hospital (Singapore) Cytogenetics department for karyotype analyses.

Immunofluorescence

Cells were washed with DPBS and then fixed in 4% PFA for 20 min at RT. PFA was removed and cells were washed with DPBS before they were blocked and permeabilized in blocking buffer (10% donkey serum, 0.1% Triton X-100 in DPBS) for 1h at RT. Cells were then incubated with primary antibodies diluted in staining buffer (1% donkey serum, 0.1% Triton X-100 in DPBS) overnight at 4°C. Excess primary antibodies were removed and the cells were washed 3 times with DPBS before incubation with fluorescence-conjugated secondary antibodies diluted in staining buffer for 1 h in the dark at RT. Cells were washed 3 times with DPBS to remove excess and unbound antibodies. NucBlue Fixed Cell ReadyProbes Reagent (DAPI, ThermoFisher Scientific) diluted in DPBS at 1 drop/ml was then added to each well. Cells were imaged using the Leica FV-3000. ImageJ was used for image processing and analysis. Primary antibodies (see [key resources table](#)) used are rabbit anti-CCNO (Atlas, 1:500); rabbit anti-HA (1:1000); goat anti-Nanog (1:100); mouse anti-AFP (1:1000); mouse anti-SMA (1:1000); mouse anti-TUJ1 (1:1000). Secondary antibodies are species-specific Alexa Fluor secondary antibodies (1:1000; see [key resources table](#)).

RNA extraction, cDNA synthesis and quantitative real-time PCR (qPCR)

Qiagen RNeasy kit was used to extract total RNA from cells. 500 ng of purified RNA was converted into cDNA using the High-Capacity cDNA Reverse Transcription Kit (Applied Biosystems). QPCR was performed using the QuantStudio 7 Flex Real-Time PCR System with samples run in duplicates and normalized to housekeeping gene ACTB. Primer sequences are listed in the [key resources table](#). Adult lung mRNA used as a positive control for QPCR experiments was obtained from Biochain (Total RNA – Human Adult Normal Tissue: Lung lower left lobe; Cat #R1234152-50; Lot #B6050780).

Protein extraction and western blot

Whole cell lysates were prepared by lysing cells in Pierce RIPA buffer (ThermoFisher Scientific) supplemented with complete protease inhibitor cocktail (Calbiochem). 10 µg protein was resolved on a 7.5% SDS PAGE gel and then transferred onto PVDF membranes via semi-dry transfer method (Bio-rad). Membranes were blocked in 5% skim milk in Tris-buffered saline (TBST: 0.05 M Tris, 0.138 M NaCl, 0.0027 M KCl, pH 8.0) with 0.1% Tween 20 (Sigma-Aldrich) for 1h at RT. Membranes were then incubated with primary antibodies at 4°C overnight. Membranes were then washed 3 times in TBST and then incubated with HRP-linked secondary antibodies for 1h at RT. Membranes were washed 3 times with TBST before proteins were visualized using the SuperSignal West Femto Maximum Sensitivity Substrate (ThermoFisher Scientific) on the Chemidoc (Bio-rad). Primary antibodies (see [key resources table](#)) used are rabbit anti-CCNO (Atlas, 1:500); rabbit anti-HA (1:1000); mouse anti-β-tubulin (1:1000).

Differentiation of hESCs into lung progenitors

H9 cells were dissociated into single cells with Accutase for 5 min at 37°C. 400,000 cells were seeded into each well of a 12-well plate and left in the incubator to attach overnight. Cells were fed fresh E8 media the next day (Day –1, D-1). At D0, H9 cells were differentiated into definitive endoderm (DE) cells using a protocol previously published by Vallier et al.⁹⁰ Briefly, on D0, cells were treated 100 ng/mL Activin A, 80 ng/mL FGF2, 10 µM LY294002, 3 µM CHIR99021, 10 ng/mL BMP4 in CDM-PVA medium. On D1, cells were treated with 100 ng/mL Activin A, 80 ng/mL FGF2, 10 µM LY294002 and 10 ng/mL BMP4 in CDM-PVA medium. On D2, cells were treated with 100 ng/mL Activin A, 80 ng/mL FGF2, 1X B27, 1X NEAA in RPMI medium. To differentiate the DE cells into anterior foregut and subsequently lung progenitors, the protocol published by McCauley et al.⁹¹ was used. To drive DE cells toward anterior foregut formation, cells were treated with 10 µM SB431542 and 2 µM Dorsomorphin (DSM) in basal medium (1X B27, 1X N2,

1X Glutamax, 1 mM HEPES in DMEM F12 Advanced) for 3 days. To differentiate AFE cells into lung progenitors, cells were treated with 3 μ M CHIR, 10 ng/mL BMP4, 10 ng/mL FGF7, 10 ng/mL FGF10 and 50 nM RA in basal medium for 9 days.

Fluorescence-activated cell sorting (FACS)

For sorting at Day 15, differentiated H9 cells were washed once with DPBS and then dissociated into single cells with TryPLE express. TrypLE express was diluted out with DMEM Advanced F12 and removed by centrifugation at 1200 rpm for 5 min. The cell pellet was resuspended in FACS buffer supplemented with 2% penicillin/streptomycin and 10 μ M Y-27632. The cell suspension was passed through a 40 μ m cell strainer to remove cell clumps before cells were counted using the Scepter Cell Counter (Merck Millipore). Cell concentration was adjusted to 1 million cells/100 μ L FACS buffer. 0.5 μ L isotype control or 0.5 μ L Human ALCAM/CD166 Phycoerythrin (PE)-conjugated antibody (Clone 105902) (R&D Systems) was added per 100 μ L. Cells were stained for 30 min in the dark at 4°C. Excess antibodies were diluted out and removed by adding FACS buffer followed by centrifugation at 1200 rpm for 5 min. Cell pellets were resuspended in 500 μ L FACS buffer. Samples were FACS sorted with the unstained and isotype-stained H9-derived lung progenitors as a negative control for the gating parameters.

For sorting at Day 25–30 to collect airway basal cells, lung organoids embedded in Matrigel were washed with DPBS once. Organoids were then incubated with TrypLE express for 30 min at 37°C. DMEM F12 advanced was used to dilute out TrypLE express and then cells were collected into a pellet by centrifugation at 1200 rpm for 5 min. The cells were resuspended in FACS buffer supplemented with 2% penicillin/streptomycin and 10 μ M Y-27632, passed through a 40 μ m cell strainer. Cells were counted and cell concentration was adjusted to 1 million cells/100 μ L FACS buffer. 0.5 μ L of each isotype control or 0.5 μ L Human NGFR (APC)-conjugated antibody and 0.5 μ L EpcAM (PE)-conjugated antibody were added per 100 μ L. Cells were stained for 30 min in the dark at 4°C. Excess antibodies were diluted out and removed by adding FACS buffer followed by centrifugation at 1200 rpm for 5 min.

Cell pellets were resuspended in 500 μ L FACS buffer prior to FACS sorting. Unstained and isotype-stained H9-derived lung cells were used as negative controls for the gating parameters.

Proximal lung organoid culture

To obtain proximal lung organoids, a protocol published by Hawkins et al., 2021 was used. Briefly, Day 15-sorted CD166+ cells were resuspended in basal medium containing 250 ng/mL FGF2, 100 ng/mL FGF10, 50 nM Dexamethasone (Sigma-Aldrich), 0.1 mM 8-Bromoadenosine 30,50-cyclic monophosphate sodium salt (cAMP, Sigma-Aldrich) and 0.1 mM 3-Isobutyl-1-methylxanthine (IBMX) (Sigma-Aldrich). Undiluted growth factor-reduced Matrigel (Corning) was added to the cell suspension at a 1:1 ratio after which 40 μ L of this cell suspension was added to the middle of each 24-well plate to create a Matrigel drop. The plates were then returned to the incubator to allow the Matrigel drops to solidify for at least 30 min before medium is overlaid over the drops. Y-27632 was included in the medium for the first 24 h to improve cell survival. Medium was refreshed every other day for ~2 weeks before proximal lung organoids were harvested for cell sorting.

Terminal differentiation of ESC-derived basal cells

150,000 cells were seeded onto 6.5 mm Matrigel-coated Transwell inserts. When cells reached 100% confluence, media was removed from both chambers and PneumaCULT ALI medium (Stem Cell Technologies) was added only to the bottom chamber. Medium was refreshed every other day for 2 weeks before cells were harvested for mRNA or fixed in 4% PFA or methanol for immunostaining.

Western blotting to detect endogenous CCNO from ALI cultured hESCs

6 transwells of wild type or CCNO mutant cells, respectively, were lysed with 300 μ L RIPA buffer (Thermo Fisher Scientific). The cell lysates were sonicated for 10 s and spun down for 15 min at 12000 g. 200 μ L cell lysate was boiled with 200 μ L SDS loading buffer. Subsequently, the cell lysates were separated on SDS-PAGE gels, transferred to PVDF membrane and incubated with blocking buffer (3% BSA, 0.1% Tween in PBS). Previously validated rabbit anti-CCNO antibody (Atlas HPA050090, validated in Wallmeier et al.¹⁸) was used for detection of endogenous CCNO protein.

Immunofluorescence staining of ALI cultured hESCs and microscopy

Cells grown on transwells were fixed with ice-cold methanol at -20°C for 15 min. Cells were then blocked with blocking buffer (3% bovine serum albumin in PBS) for 1 h, followed by 1 h incubation with relevant primary antibodies (see [key resources table](#)): anti-foxj1 antibody (1:200); anti-RFX2 antibody (1:200); anti-RFX3 antibody (1:200), rabbit anti Deup1 (1:200), mouse IgG2b anti SAS6 (1:200), at room temperature. After three washes with wash buffer (0.1% Triton in PBS), cells were incubated with secondary antibodies and DAPI for 1 h. After three washes with wash buffer, the stained cells were mounted on glass slides with fluorescence-mounting medium and imaged with an Olympus Fluoview upright laser confocal microscope.

Transmission electron microscopy on human respiratory cells

Patients A to I

Samples of airway epithelial cells were obtained from nasal or bronchial biopsies of patients. They were fixed by 2.5% glutaraldehyde in 0.045 M cacodylate buffer, pH 7.4, for a period of 2 h at a temperature of 4°C. Subsequently, the samples were postfixed with osmium tetroxide (OsO_4) and processed for transmission electron microscopy in accordance with standard procedures. The ultrathin sections were examined at different magnification of 6,000 to 100,000). Patient information is listed in [Tables S1](#) and [S2](#).

Patients J to T

Respiratory epithelial cells were obtained by nasal brush biopsies from the middle turbinate with nasal biopsy brushes (Engelbrecht Medicine and Laboratory technology). For transmission electron microscopy analyses, airway cells were directly suspended in 2.5%

glutaraldehyde and were fixed overnight at 4°C. Afterward, cells were stained with 1% osmium tetroxide. For complete permeabilization, the stained material was then incubated overnight at 4°C with a 1,2-epoxypropane-epone mixture in a 1:1 ratio. The samples were then embedded in epon, before they were transferred onto copper grids. Contrasted with uranyl acetate and Reynold's lead citrate sample material was finally visualized using the Philips CM10 microscope. Patient information is listed in [Table S2](#).

QUANTIFICATION AND STATISTICAL ANALYSIS

Quantification, image and statistical analyses were performed with ImageJ Excel, and GraphPad Prism software. Images used for intensity quantification were all taken with the same microscopy parameters. Nuclear and cytoplasmic intensity was measured using an in-house built ImageJ macro. Hoechst staining was segmented using morphological filtering and the segmented nucleus area was used to measure the mean fluorescence intensity of the channel of interest per nucleus. Cytoplasmic fluorescence intensity quantifications were performed by manual outlining of the cellular fluorescence signal. Nuclear and cytoplasmic measurements were then classified based on differentiation stages and divided by the mean value per coverslip of the centrosome stage signal and normalized as that $y = 0$ corresponds to the mean centrosome stage intensity.

Data were obtained from at least three independent experiments unless differently stated. Information about the statistical analysis and the tests used in each case can be found in the figure legends. Kruskal-Wallis test + Dunn's multiple comparisons, two-tailed Mann-Whitney U-test and two-sided Chi-square test (two-proportion z-test) were performed and p -values summarized using **** (p -value <0.0001).

ADDITIONAL RESOURCES

Patients OI-66 II1 and OI-104 II1 were recruited as part of the multicenter prospective National Israeli Consortium study on PCD, held by 14 specialty groups in Israel. Institutional Review Boards for each site approved the study and all patients and guardians provided written informed consent. The study was registered with [ClinicalTrials.gov](#), number NCT01070914 (<https://www.clinicaltrials.gov/study/NCT01070914>).